

Spin Textures induced by Quenched Disorder in a Reentrant Spin Glass: Vortices versus "Frustrated" Skyrmions

I. Mirebeau,^{1,*} N. Martin,¹ M. Deutsch,² L. J. Bannenberg,³ C. Pappas,³ G. Chaboussant,¹ R. Cubitt,⁴ C. Decorse,⁵ and A. O. Leonov^{6,7}

¹Laboratoire Léon Brillouin, CEA, CNRS, Université Paris-Saclay, CEA Saclay 91191 Gif-sur-Yvette, France

²Université de Lorraine, CNRS, CRM2, Nancy, France

³Faculty of Applied Science, Delft University of Technology, 2629 JB Delft, the Netherlands

⁴Institut Laue Langevin, BP156, F-38042 Grenoble France

⁵ICMMO, Université Paris-Sud, Université Paris-Saclay, F-91405 Orsay, France

⁶Chiral Research Center, Hiroshima University, Higashi-Hiroshima, 739-8526, Japan

⁷Department of Chemistry, Faculty of Science, Hiroshima University
Kagamiyama, Higashi Hiroshima, Hiroshima 739-8526, Japan

(Dated: July 4, 2018)

Reentrant spin glasses are frustrated disordered ferromagnets developing vortex-like textures under an applied magnetic field. Our study of a $\text{Ni}_{0.81}\text{Mn}_{0.19}$ single crystal by small angle neutron scattering clarifies their internal structure and shows that these textures are randomly distributed. Spin components transverse to the magnetic field rotate over length scales of 3-15 nm in the explored field range, decreasing as field increases according to a scaling law. Monte-Carlo simulations reveal that the internal structure of the vortices is strongly distorted and differs from that assumed for "frustrated" skyrmions, built upon a competition between symmetric exchange interactions. Isolated vortices have small non-integer topological charge. The vortices keep an anisotropic shape on a 3 dimensional lattice, recalling "croutons" in a "ferromagnetic soup". Their size and number can be tuned *independently* by the magnetic field and concentration x (or heat treatment), respectively. This opens an original route to understand and control the influence of quenched disorder in systems hosting non trivial spin textures.

Disorder plays a central role in the advent of the most spectacular quantum phenomena observed in condensed matter. The quantum Hall effect observed in a two-dimensional (2d) electron gas^{1,2}, the two-current character of the resistivity in impurity-containing ferromagnetic metals³ leading to giant magneto-resistance⁴ or the dissipationless conduction observed in the mixed state of type II superconductors^{5,6} are prominent examples. Frustrated ferromagnets represent another type of playground to study the influence of disorder. Such systems show competing ferromagnetic (FM)/antiferromagnetic (AFM) interactions combined with atomic disorder. The influence of quenched disorder, when treated in a mean field model with infinite range interactions^{7,8}, leads to a canonical spin glass (SG) when the average interaction \bar{J} is smaller than the width of the interaction distribution or to a reentrant spin glass (RSG) otherwise. Here, we focus on the FM case ($\bar{J} > 0$) of the RSGs where vortex-like textures are stabilized under an applied magnetic field at low temperature. We study their morphology and spatial organization by combining neutron scattering experiments on a $\text{Ni}_{0.81}\text{Mn}_{0.19}$ single crystal and Monte Carlo simulations. We compare them with those expected for skyrmions built upon a competition between symmetric exchange interactions. Altogether, our study shows that one can *independently* tune the number and size of vortex textures in frustrated disordered magnets with the magnetic field, heat treatment and concentration of magnetic species. It provides clues to control and use the influence of quenched disorder in frustrated ferromagnets and skyrmion-hosting systems in bulk state.

I. REENTRANT SPIN GLASSES AND "FRUSTRATED" SKYRMIONS

As a common feature, RSGs show three successive phase transitions upon cooling: a paramagnetic to FM transition at T_C followed by transitions towards two mixed phases at T_K and T_F . Below the canting temperature T_K spin components \mathbf{m}_T transverse to the longitudinal magnetization \mathbf{m}_L start to freeze. The lower temperature T_F marks the onset of strong irreversibilities of \mathbf{m}_L . In this picture, the ferromagnetic long range order of \mathbf{m}_L is preserved in the RSG down to $T \rightarrow 0\text{K}$. The phase diagram (T, x) where x is a parameter tuning the distribution of interactions shows a critical line between SG and RSGs ended by a multicritical point at x_C where all phases collapse⁸. Metallic ferromagnetic alloys with competing nearest-neighbor interactions tuned by the concentration x show a magnetic phase diagram (T, x) in qualitative agreement with mean field predictions. Well-known examples are $\text{Ni}_{1-x}\text{Mn}_x$ ⁹, $\text{Au}_{1-x}\text{Fe}_x$ ¹⁰, $\text{Fe}_{1-x}\text{Al}_x$ ^{11,12} and $\text{Fe}_{1-x}\text{Cr}_x$ ¹³ crystalline alloys or amorphous Fe-based alloys¹⁴⁻¹⁸. A large body of experimental and theoretical studies have revealed the peculiarities of their magnetic behavior.

In this paper, we focus on vortex-like textures observed in the 1980s in the above systems, either in single crystal, polycrystal or amorphous form^{12,19-21}. They were detected under applied magnetic field in the mixed phases of ferromagnetic, weakly frustrated alloys ($x \ll x_C$), using small angle neutron scattering (SANS), which provides a clear signature of these textures and reveals

their typical size. Inside the vortices, the transverse spin components are frozen in the plane perpendicular to the applied field, and they are rotated over a finite length scale, yielding a maximum in the neutron scattering cross section versus the momentum transfer. In addition, the transverse spin freezing induces Dzyaloshinskii-Moriya (DM) anisotropy²², together with a chiral anomalous Hall effect^{23–25}. Stimulated by these measurements, Monte Carlo (MC) simulations were performed in a 2d lattice, showing similar vortex-like patterns²⁶. The knowledge of their spatial organization has however remained elusive.

In this context, it is worth recalling that ferromagnets may also host nanometric spin textures known as skyrmions (SKs). SKs form double-twist solitonic structures, offering many perspectives in spintronics and data storage^{27,28}. As predicted by theory^{29–33}, some anisotropic ordered magnets with competing nearest neighbor (NN) and next nearest neighbor (NNN) exchange interactions may host localized SKs with versatile internal structure and smooth rotation of the magnetization. Different types of modulated phases such as hexagonal or square SK lattices have been predicted, yielding a very rich phase diagram³⁰.

The size of these "frustrated" SKs, of the order of a few lattice constants, is comparable to the typical vortex size in RSGs and much smaller than the size of chiral SKs stabilized by DM anisotropy in thin films or bulk state, which is usually above 10 nm^{34,35}. Therefore, quenched disorder should affect frustrated SKs much more than their chiral counterparts, expected to undergo a collective pinning by disordered impurities without deep changes of their internal structure³⁶. Experimentally, large SK lattices were observed in non-centrosymmetric frustrated alloys with chemical disorder^{37,38}, showing magnetic anomalies similar to the RSG's. Frustrated SKs have been suspected in very few systems so far, such as Gd₂PdSi₃ (Ref. 39).

Remarkably, frustrated SKs reveal strong similarities with the vortex textures observed in RSGs. Our study attempts to clarify the subtle differences between these two types of topological defects. To that end, we report on new experiments performed on a weakly frustrated Ni_{0.81}Mn_{0.19} single crystal, searching for a vortex lattice and aiming for a better characterization of these field-induced magnetic textures (Section II). Our experiments are complemented by MC simulations with a minimal model, which clarifies the internal structure of the vortices and identifies their most relevant features (Section III). We discuss the origin of the vortex textures, and compare them with SKs, either chiral or frustrated, observed in bulk materials (Section IV).

II. VORTEX-LIKE TEXTURES IN A SINGLE CRYSTALLINE REENTRANT SPIN GLASS

A. The Ni_{1-x}Mn_x system and studied sample

In Ni_{1-x}Mn_x alloys, magnetic frustration arises from competing interactions between NN pairs, namely the AFM Mn-Mn pairs and the FM Ni-Mn and Ni-Ni pairs^{43,44}. The NNN Mn-Mn pairs are FM. The multicritical line between RSG and SG phases is located around $x_C = 0.24$, close to the stoichiometric Ni₃Mn (see Refs. 40,41 and Fig. 1a). Strikingly, the Ni₃Mn ordered superstructure of $L1_2$ type and space group $Pm\bar{3}m$ eliminates all NN Mn-Mn pairs. This offers the possibility of tuning the magnetic order by controlling the number of such pairs through an appropriate heat treatment^{45–47}. The fully ordered Ni₃Mn is a ferromagnet with a Curie temperature $T_C \sim 450$ K, whereas a disordered alloy of the same composition (space group $Fm\bar{3}m$) is a spin glass with a freezing temperature $T_F \sim 115$ K.

Here, we study a Ni_{0.81}Mn_{0.19} single crystal, already used for the neutron scattering experiments presented in Ref. 21. The single crystal form limits the distributions of magnetocrystalline anisotropies and demagnetizing fields within the sample, and provides the best playground to search for a vortex lattice. A thin rectangular plate was cut from the large crystal in a (110) plane for magnetic measurements. Both samples were heated at 900 °C during 20 hours in a sealed quartz tube under vacuum, then quenched into an ice and water mixture to ensure maximal disorder⁴¹. They were stored in liquid nitrogen between experiments to prevent any further evolution of the short range order.

Static magnetic susceptibility was measured versus temperature under a field $H = 20$ Oe in both field cooled (FC) and zero field cooled (ZFC) conditions, using a superconducting quantum interference device (SQUID). With decreasing temperature, the ZFC susceptibility strongly increases at the Curie temperature $T_C = 257$ K, shows a plateau over an extended temperature range as expected for weakly frustrated RSGs, and then decreases (Fig. 1b). The freezing temperature $T_F = 18$ K, defined similarly to T_C by the inflection point of the susceptibility versus temperature in the ZFC state, locates the onset of *strong* magnetic irreversibilities. The ratio $T_F/T_C \simeq 0.07$ characterizes the weak frustration of our sample. The canting temperature $T_K \sim 120$ K which situates between T_C and T_F locates much weaker irreversibilities related to transverse spin freezing. It was determined by previous neutron scattering experiments²⁰. The three characteristic temperatures merge at the critical point.

B. Small-angle neutron scattering

SANS measurements were performed on the D33 instrument of the Institut Laue Langevin (ILL), using an

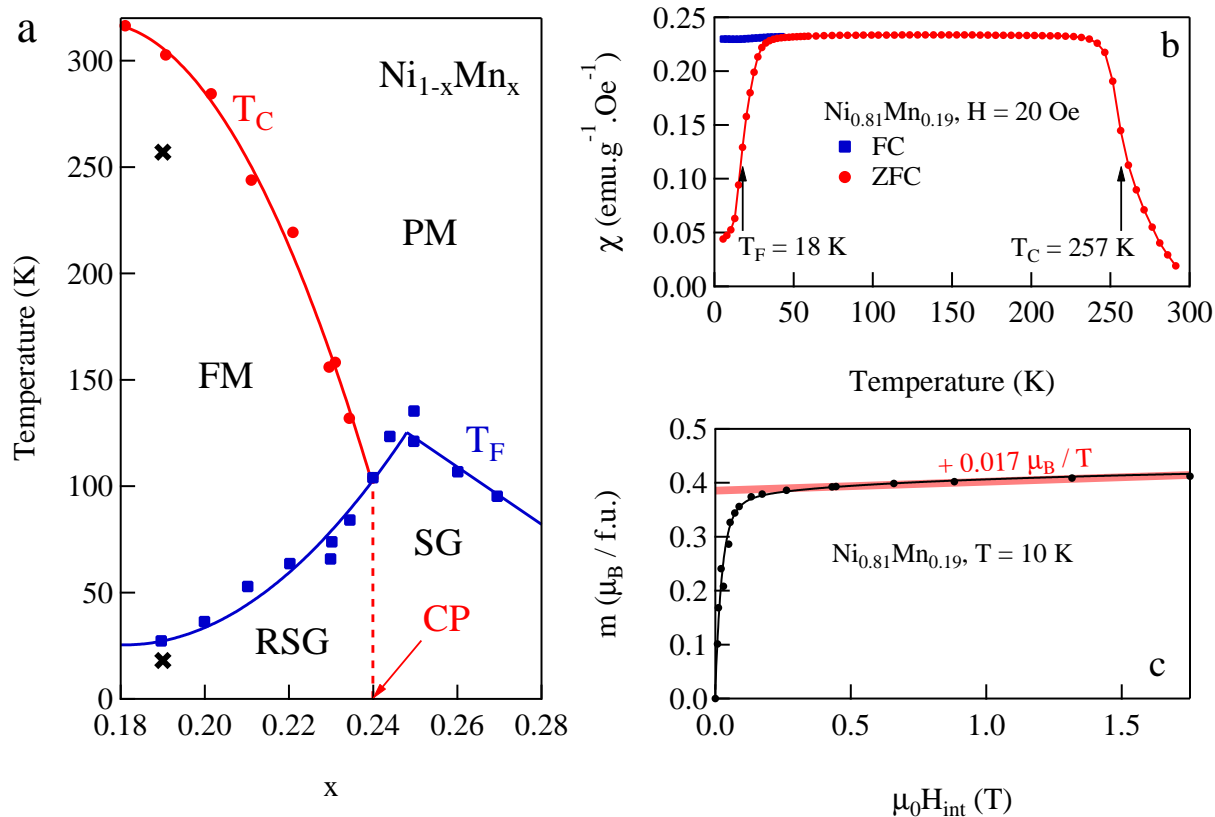


FIG. 1: (a) Magnetic phase diagram of the disordered $\text{Ni}_{1-x}\text{Mn}_x$ system determined by bulk magnetic measurements and adapted from Ref. 40. A critical point (CP) occurs for $x \sim 0.24$, see Ref. 41. (b) Static susceptibility χ of the $\text{Ni}_{0.81}\text{Mn}_{0.19}$ sample -initially zero field cooled down to 4.2 K- recorded upon warming under a magnetic field of 20 Oe (ZFC, red circles) then upon cooling under field (FC, blue squares). The characteristic freezing ($T_F \sim 18$ K) and Curie ($T_C \sim 257$ K) temperatures are obtained from the extrema of the temperature derivative of χ and reported in (a) (black crosses). (c) Field-dependence of the magnetization of $\text{Ni}_{0.81}\text{Mn}_{0.19}$ (reproduced from Ref. 42). After a quick rise, m tends to saturate and further evolves with a small, yet finite, slope (red line).

incident neutron wavelength $\lambda = 6 \text{ \AA}$ and a sample to detector distance $D = 2.8$ m. Data were corrected for the detector efficiency and calibrated cross sections were obtained by taking the sample thickness and transmission, as well as the incident neutron flux, into account⁴⁸. A magnetic field H up to 2 T was applied to the sample, in two configurations (see Fig. 2): *a*) along the neutron beam, which defines the y axis; *b*) along the x axis perpendicular to the neutron beam, namely in a plane parallel to the detector (x, z) plane. Additional measurements were performed in configuration *b*) on the PAXY spectrometer of the Laboratoire Léon Brillouin (LLB) under a magnetic field up to 8 T for the same neutron wavelength and sample-to-detector distance. Fig. 2 shows typical intensity maps recorded in the detector plane for the two configurations. The intensity is measured at 3 K in the ZFC state under a magnetic field $H = 2$ T, which almost saturates the sample magnetization (Fig. 1c).

In configuration *a*), the intensity distribution does not show any Bragg spot, rather a broad maximum at a finite momentum transfer. The intensity is isotropically

distributed over a ring of scattering in the detector plane. The absence of any Bragg spots strikingly contrasts with the scattering patterns in SK lattices or superconducting flux line lattices observed in single crystal samples for the same experimental configuration^{49,50}. It means that although the sample is single crystalline, the magnetic defects are organized in a random or liquid-like way. As discussed below, this is due to the random occupation of the lattice sites and subsequent disorder of Mn-Mn NN AFM bonds.

In configuration *b*), one observes a similar pattern, but the intensity is now modulated according to the orientation of the momentum transfer with respect to the applied field, and is strongly enhanced in the direction $\mathbf{q} \parallel \mathbf{H}$. This modulation comes from the selection rule for magnetic neutron scattering, which impose that only the spin components perpendicular to the scattering vector \mathbf{q} contribute to the magnetic cross-section. As schematically explained in Fig. 2 the dominant contribution to the scattering in this configuration arises from spin components \mathbf{m}_T transverse to the magnetic field. In the fol-

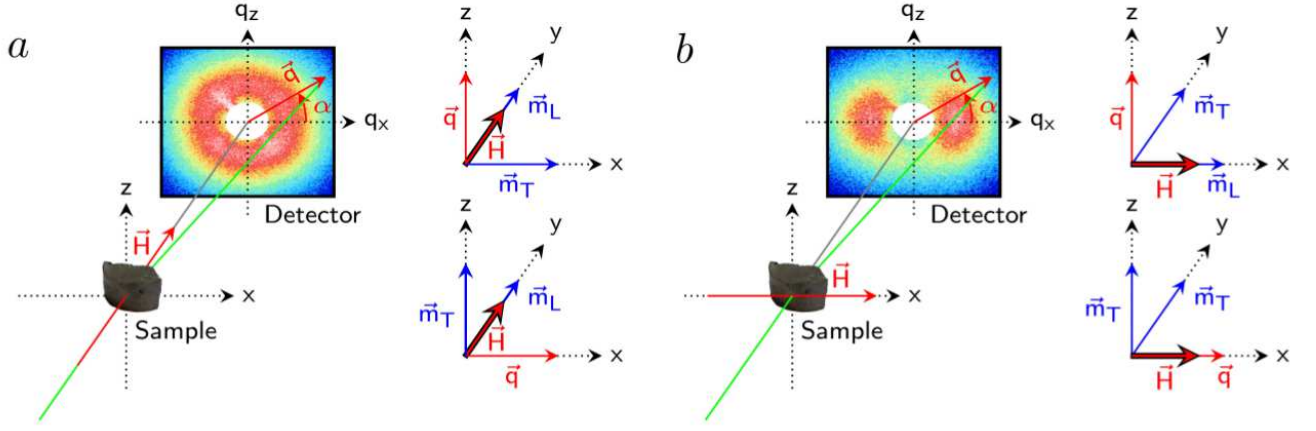


FIG. 2: Schematic configurations of the SANS experiments with the applied magnetic field \mathbf{H} parallel to the neutron beam (a) and with \mathbf{H} parallel to the detector plane (b). Orientations of the transverse \mathbf{m}_T and longitudinal \mathbf{m}_L spin components are shown in each case which, combined to the selection rules of magnetic neutron scattering (Eq. 1), lead to the corresponding patterns (here recorded at $T = 3$ K and $H = 2$ T after zero-field cooling). In both configurations, the magnetic field is applied along the [110] (or equivalent) crystallographic direction.

lowing analysis, we focus on this configuration, which allows us to better characterize the spin textures. The intensity maps in configuration b) can be described as

$$\sigma(q, \alpha) = \sigma_L(q) \cdot \sin^2 \alpha + \sigma_T(q) \cdot (1 + \cos^2 \alpha) + I_{bg}(q) \quad , \quad (1)$$

where α is the angle (\mathbf{q}, \mathbf{H}), $\sigma_L(q)$ and $\sigma_T(q)$ are the magnetic scattering cross sections related to correlations between transverse and longitudinal spin components, respectively. $I_{bg}(q)$ is an isotropic background which consists of a low- q contribution from crystal inhomogeneities and a constant term which can be calculated exactly, and which is in excellent agreement with experiment (see details in Ref. 48). Noticing that Eq. 1 fits the angular dependence of the intensity, we average the scattering map within two angular sectors of 60° : sector 1 for $\mathbf{q} \parallel \mathbf{H}$ ($\alpha = 0^\circ$) and sector 2 for $\mathbf{q} \perp \mathbf{H}$ ($\alpha = 90^\circ$) (see Fig. 3 a,b and c). We then combine the intensities from the two sectors to separate the contributions from the transverse and the longitudinal spin components (Fig. 3d).

As a key result, the intensity from the transverse spin components $\sigma_T(q)$ shows a clear maximum in q , which arises from the vortex-like textures. As shown below, the FM correlated transverse spin components rotate over a finite length scale to compensate the transverse magnetization, yielding negligible intensity at $q = 0$ and a maximum related to the vortex size. When the field increases, the maximum intensity decreases and its position moves towards high q values (Fig. 4b). A signal from the transverse spin components is observed up to the highest field of 8 T. On the other hand, the intensity from the longitudinal spin components $\sigma_L(q)$ shows no well-defined maximum at $q \neq 0$ (Fig. 4a). Above 2 T, it becomes very small and difficult to separate from the background

contribution⁴⁸.

In a first step, the transverse cross section was fitted by the phenomenological expression

$$\sigma_T(q) = \frac{\sigma_M \kappa q}{2\pi q_0} \cdot \left(\frac{1}{\kappa^2 + (q - q_0)^2} - \frac{1}{\kappa^2 + (q + q_0)^2} \right) + \frac{I_{bg}(q)}{2} \quad , \quad (2)$$

where the first term accounts for the observed peak in the scattering cross section while the second one is related to the background. From Eq. 2, one can extract the peak position $q_{max} = \sqrt{q_0^2 + \kappa^2}$ and the integrated cross section σ_M . As shown in Fig. 4c-f, these quantities vary continuously with the magnetic field.

To interpret these results, we take into account the liquid-like order of the defects in analogy with chemical inhomogeneities. Having fitted and subtracted the background term, we express the scattering cross section as

$$\sigma_T(q) = a \Delta\rho_{mag}^2 N_d V_d^2 \times \{ \langle F_T^2(q) \rangle - \langle F_T(q) \rangle^2 \cdot [1 - S_{int}(q)] \} \quad , \quad (3)$$

where $F_T(q)$ is the normalized form factor of the defects, associated with transverse spin components, and $S_{int}(q)$ is an interference function which takes into account the local correlations between two defects. In Eq. 3, $\langle \rangle$ denotes the statistical average over the sample. $\Delta\rho_{mag} \simeq |\mathbf{m}_T|$ is the magnetic contrast between a vortex (where $|\mathbf{m}_T| \neq 0$) and the surrounding ferromagnetic region (where $|\mathbf{m}_T| \rightarrow 0$). N_d and V_d are respectively the number of vortices and their volume, and a is a constant.

In the following, we neglect the local magnetic interaction between defects. This assumption of independent

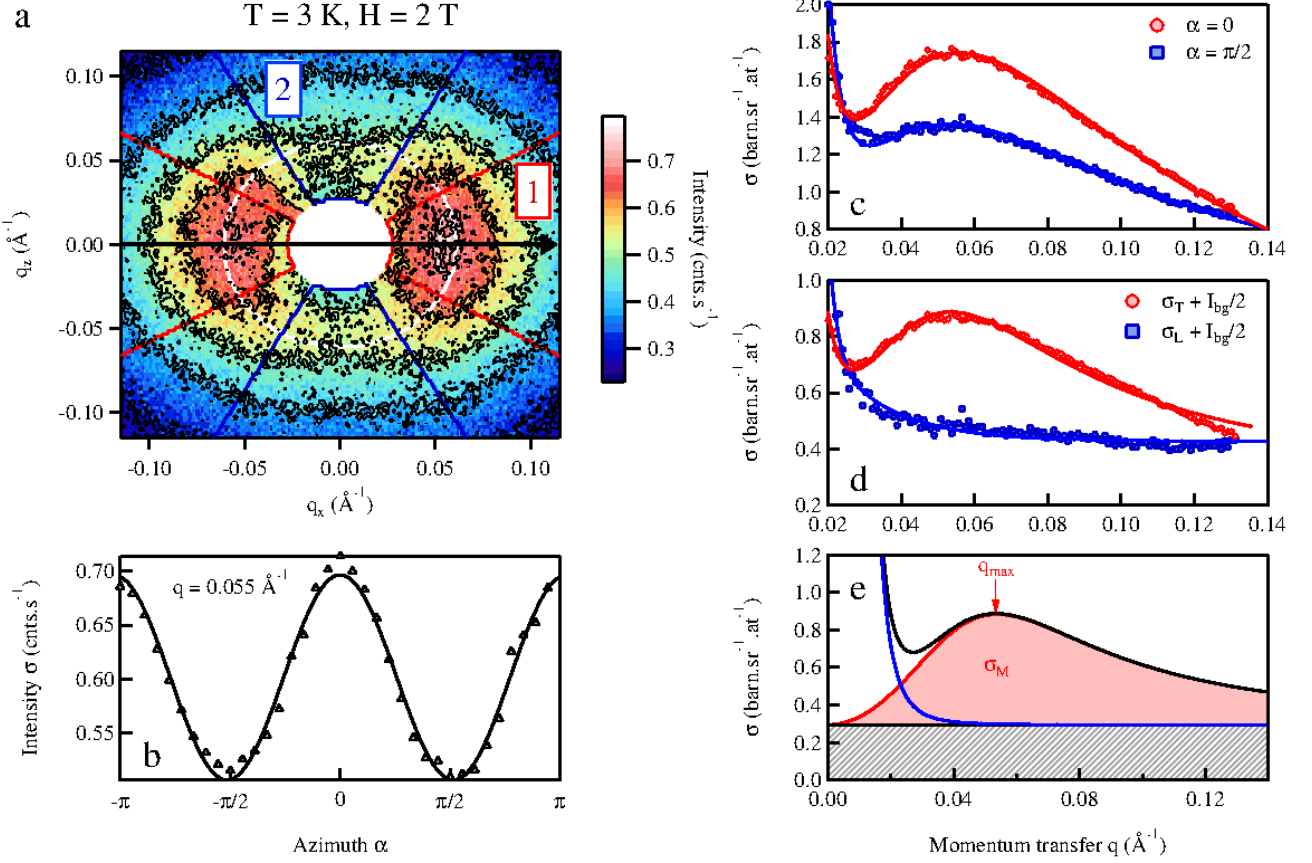


FIG. 3: **(a)** Scattering map recorded at $T = 3$ K under a field $H = 2$ T applied perpendicular to the incident beam (black arrow). The two 60° angular ranges associated with $\mathbf{q} \parallel \mathbf{H}$ (red sector 1) and $\mathbf{q} \perp \mathbf{H}$ (blue sector 2) are also shown. **(b)** Angular dependence of the intensity at a momentum transfer $q = 0.055 \text{ \AA}^{-1}$ (*i.e.* collected along the white circular trace in **(a)**). Solid line is a fit of Eq. 1 to the data. **(c)** q -dependence of the scattering cross section for momentum transfers along (red circles) and perpendicular (blue squares) to the applied field. Solid lines with corresponding colors are fits of Eq. 2 to the data. **(d)** q -dependence of the longitudinal (σ_T) and transverse (σ_L) magnetic cross sections, obtained by linear combinations of Eq. 1 for $\alpha = 0$ ($\mathbf{q} \parallel \mathbf{H}$) and $\pi/2$ ($\mathbf{q} \perp \mathbf{H}$). **(e)** Fit curve corresponding to the $\sigma_T(q)$ data of panel **(d)** (black line) along with singled out peak function (red curve) and q -dependent background signal (blue curve). The q -independent background contribution is also shown (hatched area, see text and Ref. 48).

objects is justified for a weakly frustrated system where the vortex centers are randomly distributed and located far away from each other (*i.e.* $S_{\text{int}}(q) = 1$ in Eq. 3). This assumption also holds for a system with concentrated defects, taking into account the specific form factor of the magnetic vortices and the random orientation of the transverse spin components from one vortex to another (*i.e.* $\langle F_T(q) \rangle = 0$ in Eq. 3). It is confirmed by analytical calculations of model form factors⁴⁸ and by MC simulations reported in Section III.

For independent defects, the q -dependence of the neutron intensity reduces to that of the average squared form factor, and the position q_{max} of the intensity maximum is inversely proportional to the typical size of the vortices. The integrated intensity σ_M is proportional to $\Delta\rho_{\text{mag}}^2 N_d V_d^2$, according to Eq. 3. As a toy model, we have considered regular vortices of radius r_d having an antiferromagnetic core⁴⁸. The squared form factor aver-

aged over all orientations for the transverse components has a non symmetric line shape recalling the experimental one, with a maximum at $q_{\text{max}} = \pi/r_d$.

Therefore, taking into account corrections for the demagnetization factor, the field dependence of q_{max} reflects the decrease of the vortex typical radius $r_d = \pi/q_{\text{max}}$ with increasing field⁴⁸. Over the explored field range, r_d obeys the simple relation $r_d \propto H^{-1/2}$ (Fig. 4e). The corresponding variation of $\sigma_M \propto H^{-1/2}$ suggests that the evolution of the defect shape versus the magnetic field occurs in a self similar way, yielding scaling laws for the position, width and intensity of the magnetic signal (Fig. 4b). Such laws are actually quite general and, for instance, govern the evolution of the cluster size with annealing time in metallic alloys which tend to segregate when they are quenched in the region of spinodal decomposition⁵¹.

Using Eq. 3, one can also infer the field-dependence

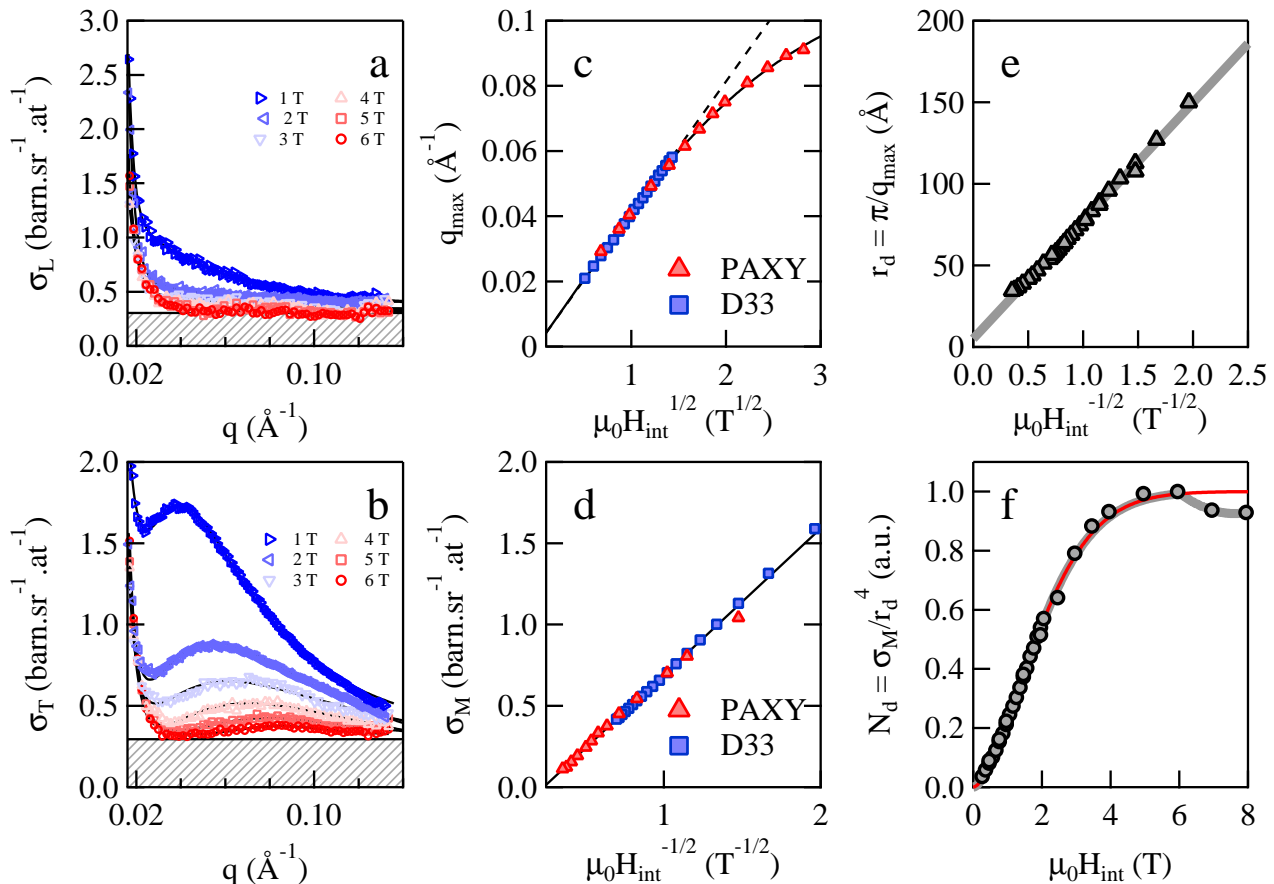


FIG. 4: Evolution of the longitudinal (a) and transverse (b) magnetic neutron scattering cross sections as a function of magnetic field. In both panels, the hatched areas represent the q -independent background contribution (see text and Ref. 48). Field-dependence of the peak position q_{\max} (c) and integrated scattering intensity σ_M (d) as obtained from a fit of Eq. 2 to the SANS data from D33 (blue squares) and PAXY (red triangles). (e) Field-dependence of the defect size r_d , computed using data of panel (c). (f) Field-dependence of the number of scattering centers N_d , as seen by SANS. The red line is a fit of Eq. 4 to the data, in the $0 \leq \mu_0 H_{\text{int}} \leq 6$ T-range.

of the number of defects (*i.e.* scattering centers) seen by SANS from the quantity σ_M/V_d^2 . For this purpose we assume thin cylindrical defects, and consider an experimental field range $H \ll J$ where the magnetic contrast (or amplitude of the transverse spin component) is roughly field-independent. We obtain $V_d \simeq r_d^2$, thus $N_d \simeq \sigma_M/r_d^4$. As shown in Fig. 4f, N_d increases with increasing field and saturates at a finite field of $\simeq 6$ T. This variation is described by a stretched exponential

$$N_d = 1 - \exp\left(-\frac{H}{H_C}\right)^\nu \quad (4)$$

with $H_C = 2.29(3)$ T and $\nu = 1.64(4)$. This result can be understood as follows. At low fields, vortices are large enough to involve several AFM bonds. Upon an increase in field, they progressively shrink while remaining centred on isolated AFM first neighbor Mn-Mn pairs⁴⁸, the number of which is fixed by the Mn concentration and heat treatment. Consequently, the number of individual

defects N_d seen by SANS will *increase*. At higher fields, however, N_d should decrease until all defects have collapsed for fields strong enough to overcome the typical AFM exchange interaction. We indeed observe a slight decrease of N_d for $\mu_0 H_{\text{int}} \gtrsim 6$ T. However we note that the field corresponding to the exchange interaction is of the order of several 100 T and is thus well-beyond our experimental range. In turn, this regime can be conveniently explored numerically. This point is addressed in the next section, where we propose a way to verify the above scenario and extend the exploration of the vortex-like textures properties towards arbitrarily large magnetic fields.

III. MONTE CARLO SIMULATIONS

Numerical studies of the reentrance phenomena and magnetic structures of reentrant spin glasses trace back to the pioneering work of Kawamura and Tanemura^{26,52}.

They showed that a minimal model is able to reproduce the main characteristics of the magnetic textures observed in RSG's. Following their approach, we first performed MC simulations on 2d matrices containing 160×160 Heisenberg spins placed on a square lattice. While the main interaction is assumed to be FM ($J = 1$), a certain fraction c of the bonds is turned into AFM ($J = -1$). Using a spin quench algorithm, the system's ground state is found where vortex-like defects appear as metastable configurations (*i.e.* with energies slightly higher than those of the bulk FM state). For the studied concentrations $c = 5$ and 20% , individual defects (similar to vortices or pairs of vortices) are evidenced, all of them being centred around the randomly distributed AFM NN pairs (see Fig. 5 for the 5% case and Ref. 48 for further details).

In all cases, the average topological charge is $Q = 0$ but individual objects locally display a finite Q , being in some cases as large as 0.3 (*i.e.* similar values as those found for certain types of frustrated SKs³⁰). The origin of the non-integer charge is clarified by considering the relatively small size of the defects as well as their irregular shapes and distorted magnetization profiles, related to the ill-defined boundaries between vortices and the ambient FM medium. In other words, the vortex-like textures stabilized under field in RSGs feature both senses of the vector chirality, resulting in a smaller topological charge than in frustrated or chiral SKs (for which $Q = \pm 1$). Extending the MC simulations to a 3d spin matrix, it appears that the vortex-like textures keep their anisotropic shape (oblate along the field direction) in the 3d lattice and can thus be dubbed as "croutons".

As shown qualitatively on the maps displayed in Figs. 5a-c, the average number of defects decreases with increasing field H while spins are progressively aligned along its direction. The computed magnetization m (Figs. 5e) increases as the number of vortices decreases, showing a quasi plateau with finite slope versus the ratio H/J . At very high fields, of magnitude comparable to the exchange constant J , a prediction of the MC modeling is that the vortices should collapse individually, yielding microscopic plateaus of m , the amplitude of which is probably too small to be experimentally observed.

In order to compare these results with the SANS experiments of Section II, we have computed the Fourier transforms of the longitudinal and transverse spin components. The longitudinal cross section σ_L decreases monotonically with increasing q (Fig. 6a,b) whereas the transverse cross section σ_T shows a broad asymmetric peak (Fig. 6c,d). Both quantities become almost q -independent at large q values. When the field increases, the magnitude of the two simulated cross sections decreases, and a fit of Eq. 2 to the simulated σ_T -curves shows that the position of the maximum q_{\max} moves towards larger values, whereas its integrated intensity σ_M decreases. This evolution reflects a decrease of the vortex size r_d with increasing H according to a scaling law (Fig. 6e) and an apparent increase of the number of vortices

N_d following Eq. 4 with fit parameters $H_C = 1.05(5)J$ and $\nu = 2.8(1)$ (Fig. 6f). Similar to the experimental case, N_d is defined as $N_d \simeq \sigma_M/r_d^4$, where $r_d = a/q_{\max}$ with a the lattice constant of $\text{Ni}_{0.81}\text{Mn}_{0.19}$. As discussed below, these results show that a minimal model is able to capture the essential features of the observed textures.

IV. DISCUSSION

A. Spin textures in a reentrant spin glass: the "crouton" picture

The MC simulations presented above strongly reflect the experimental observations, as shown by:

- i. The shape of the magnetization curve with a finite slope at large fields (compare Fig. 1c and 5e),
- ii. The existence of defects over which the transverse magnetization is self-compensated, yielding a peak of σ_T at a finite q -value. The asymmetric q -dependence of σ_T is also reproduced, suggesting similar internal structures of the defects (compare Fig. 4b and 6c,d),
- iii. The persistence of inhomogeneities of the magnetization at the scale of the vortex size, deep inside the RSG phase, as shown by the finite longitudinal cross section σ_L centered around $q = 0$ (compare Fig. 4a and 6a,b),
- iv. The field-dependence of the defect size r_d (obtained from the q -position of the peak in σ_T), obeying scaling laws $r_d \propto H^{-\beta}$ with the same exponent $\beta = 0.5$ (compare Fig. 4e and 6e),
- v. The field-dependence of the number of individual defects N_d , increasing as a function of field following the phenomenological Eq. 4, before reaching saturation (compare Fig. 4f and 6f),
- vi. The robustness of the defects, surviving up to very large fields as compared with usual magnetic SKs (compare Fig. 4f and 6f, and see Ref. 48 for a detailed discussion).

Therefore, the simulations strongly support a description of the magnetic defects observed in $\text{Ni}_{0.81}\text{Mn}_{0.19}$ as "crouton-like" defects, induced by AFM Mn-Mn first neighbor pairs, where the transverse spin components are ferromagnetically correlated and rotate to compensate the transverse magnetization. Their magnitude decreases from the vortex center to the surroundings to accommodate the average ferromagnetic medium. As discussed below, such defect shape is compatible with the interactions generally considered for the RSGs, although other defect textures could be in principle compatible with the experiment.

The main difference between the experiment and the MC simulations is the field value at which the number

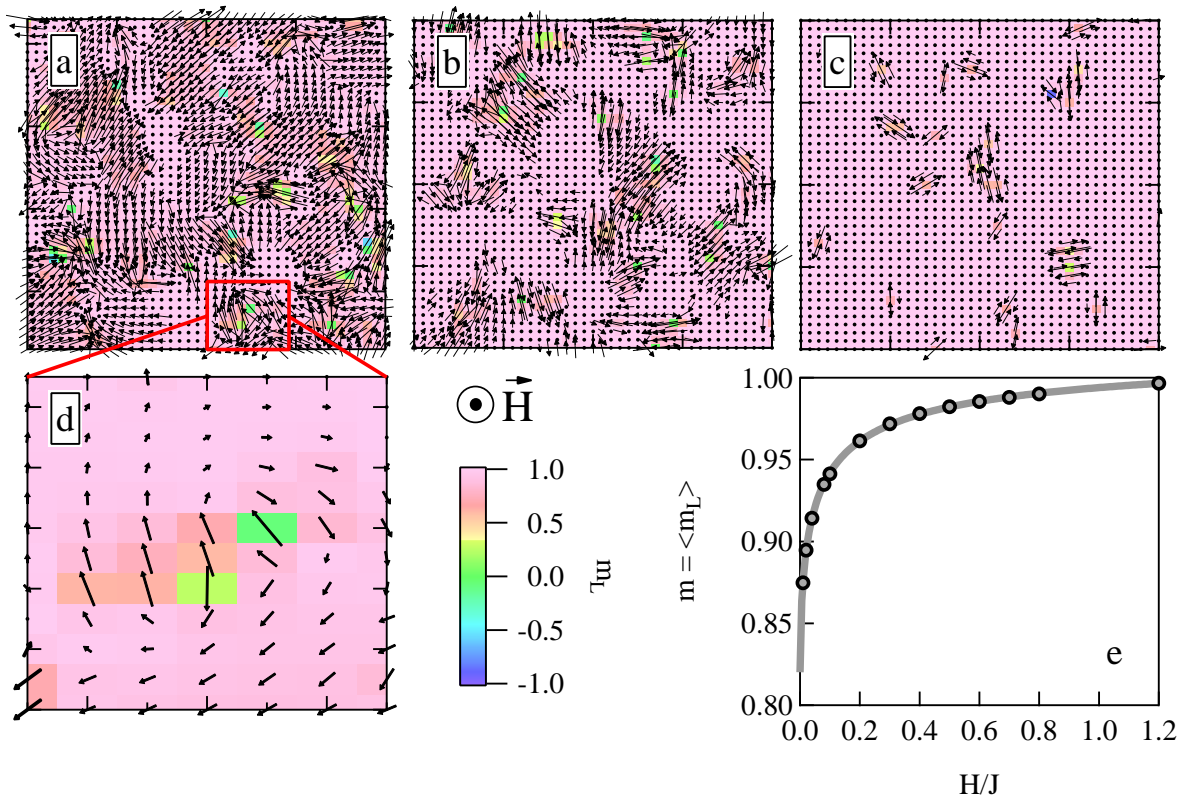


FIG. 5: Outcome of the Monte Carlo simulations for an antiferromagnetic bond concentration of 5 %. (a-c) Simulated spin maps for $H/J = 0.01, 0.1$ and 0.8 , respectively, where J is the first neighbor exchange term. We display portions of 40×40 spins for clarity. The longitudinal magnetization m_L (*i.e.* parallel to the applied field) is color-coded while the arrows represent the transverse component m_T . (d) Example of a vortex-like chiral spin circulation stabilized at $H = 0.01$ J. (e) Field-dependence of the bulk magnetization m , defined as the average value of the longitudinal magnetization per spin $\langle m_L \rangle$.

of individual defects N_d starts saturating ($H \ll J$ and $\sim J$, respectively). This suggests that an accurate determination of their stability range requires a more complex modeling, which is well-beyond the scope of the present work. Indeed, the experimental situation is complicated, involving different moments on Ni and Mn ions, 3 types of interactions, a 3d lattice with high connectivity, a high concentration of magnetic species, and an atomic short-range order (SRO). Therefore many different local environments and moment values exist in the experimental system. Comparatively, the simulations are based on a very simple case, namely a 2d square lattice with a random distribution of AFM bonds involving a single exchange constant.

Despite these differences, we stress that the agreement between both approaches is surprisingly good. Let us outline several reasons for that. Firstly, the mean field description, which identifies longitudinal and transverse spin components with different behaviors, is valid, as expected for weak frustration. The present sample behaves as a weakly frustrated ferromagnet (the ratio $T_F/T_C \simeq 0.07$ can be associated to an effective concentration of AFM bonds of $\simeq 0.07$ in mean field approximation⁴⁸),

although the concentration of first neighbor isolated Mn-Mn pairs is relatively high (in the 0.2-0.4 range depending on the amount of SRO). Experiments varying the degree of frustration through Mn content or heat treatment could check the validity of this description when approaching the critical point which separates RSG and SG phases.

Secondly, both methods involve *a statistical average of different types of defects* which do not interact with each other, but all have a typical size governed by general stability equations. This typical size is dictated by the competition between ferromagnetic exchange ($E = Jk^2$) and Zeeman energy, and it is expected to vary as $k^{-1} \propto (J/H)^{0.5}$, hence $r_d \propto H^{-0.5}$, as observed experimentally and in the simulation. Such a general law also controls the extension of Bloch walls⁵³ or soliton defects⁵⁴ among others.

Our findings also suggest that the 2d lattice provides a relevant description of the real case due to the peculiar croton shape, with much larger extension in the transverse plane than along the field axis. In 2d-XY antiferromagnets, spontaneous vortices are stabilized and undergo a Kosterlitz-Thouless transition with tempera-

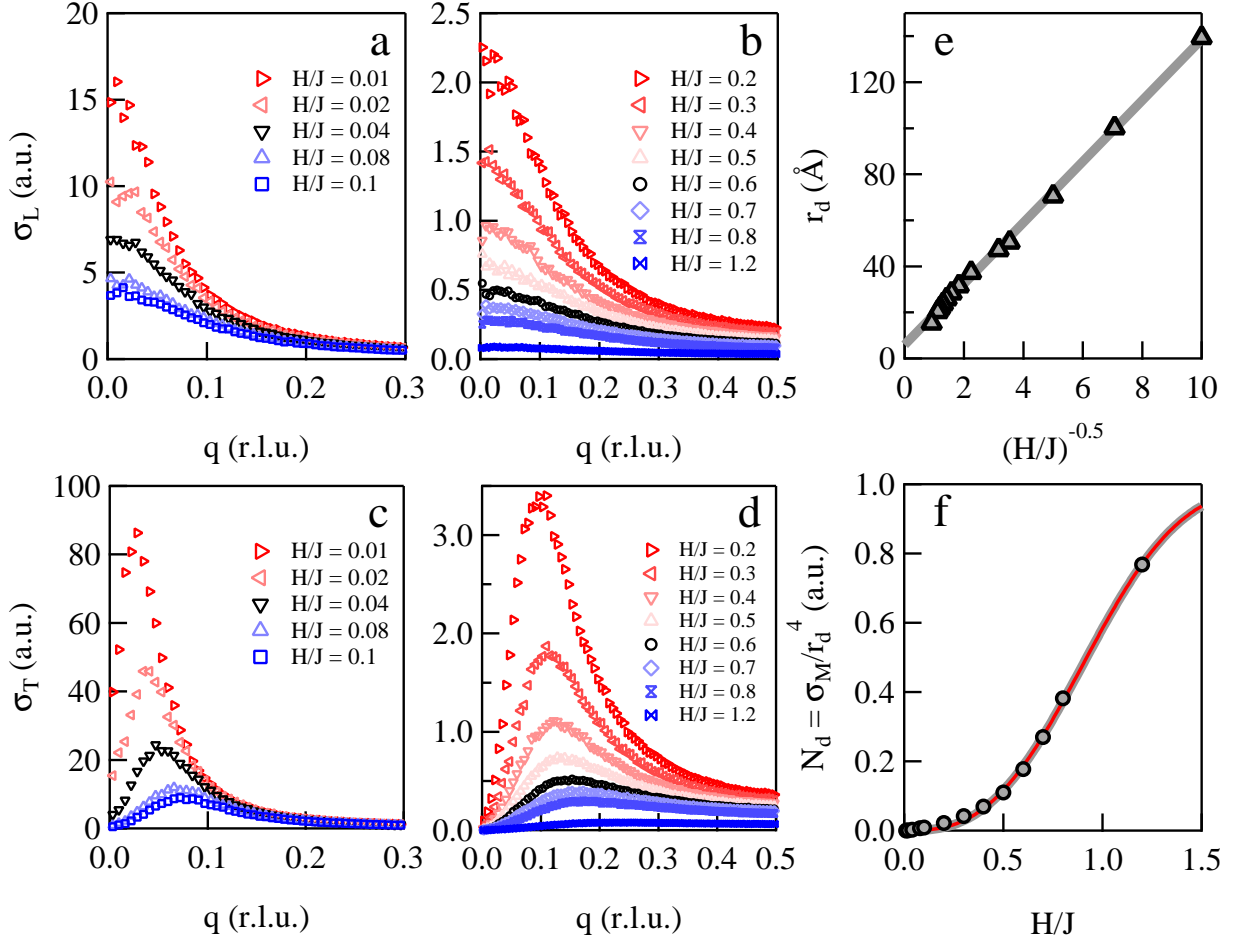


FIG. 6: Fourier analysis of the Monte Carlo results of Fig. 5. (a-d) Computed longitudinal (a,b) and transverse (c,d) form factors, obtained by Fourier transforming the calculated spin maps for different field values. The momentum q is expressed in reciprocal lattice units (r.l.u.). (e) Field-dependence of the average defect size $r_d = a/q_{\max}$, where q_{\max} is the position of the peak in σ_T and $a = 3.586 \text{ \AA}$ is the lattice constant of $\text{Ni}_{0.81}\text{Mn}_{0.19}$. (f) Field-dependence of the apparent number of defects N_d . The red line is a fit of Eq. 4 to the data, with an inflection point at $H_C = 1.05(5) J$ and a stretching exponent $\nu = 2.8(1)$.

ture, involving spontaneous symmetry breaking at a local scale^{55–57}. The reentrant transitions have a different nature, but they also involve peculiar symmetry breaking below T_K and T_F , associated to the Gabay-Toulouse and de Almeida-Thouless lines respectively⁸. As a major consequence, the transverse spin freezing and emergence of vortices strongly impact the spin excitations. A softening of the spin wave stiffness^{21,51} occurs below T_K , recalling the anomalous sound velocity in glasses^{58,59} and the spin wave softening in quasi 2d frustrated antiferromagnets⁶⁰. It is followed by a further hardening of the spin waves below T_F .

B. Vortex-like textures and skyrmions

Among the various classes of spin textures⁶¹, those studied here show clear differences with the Bloch-type

skyrmions observed in bulk chiral ferromagnets, which are primarily induced by DM anisotropy in non centrosymmetric lattices. Both occur in an average ferromagnetic medium, but the vortex-like textures probed in this study are stabilized at low temperatures, do not form a magnetic lattice and can exist for any crystal symmetry or even in amorphous compounds. This is because their primary origin is the competition of (symmetric) exchange interactions combined with site disorder, rather than antisymmetric exchange. In frustrated systems, the role of the latter, yielding DM anisotropy of chiral nature, has been investigated both theoretically^{62,63} and experimentally²². DM interactions explain the macroscopic irreversibilities in spin glasses and RSGs⁶⁴, torque measurements and paramagnetic resonance. Under field cooling conditions, they induce an additional magnetic field of unidirectional nature, which explains the slight decrease of the vortex size in NiMn when the sample

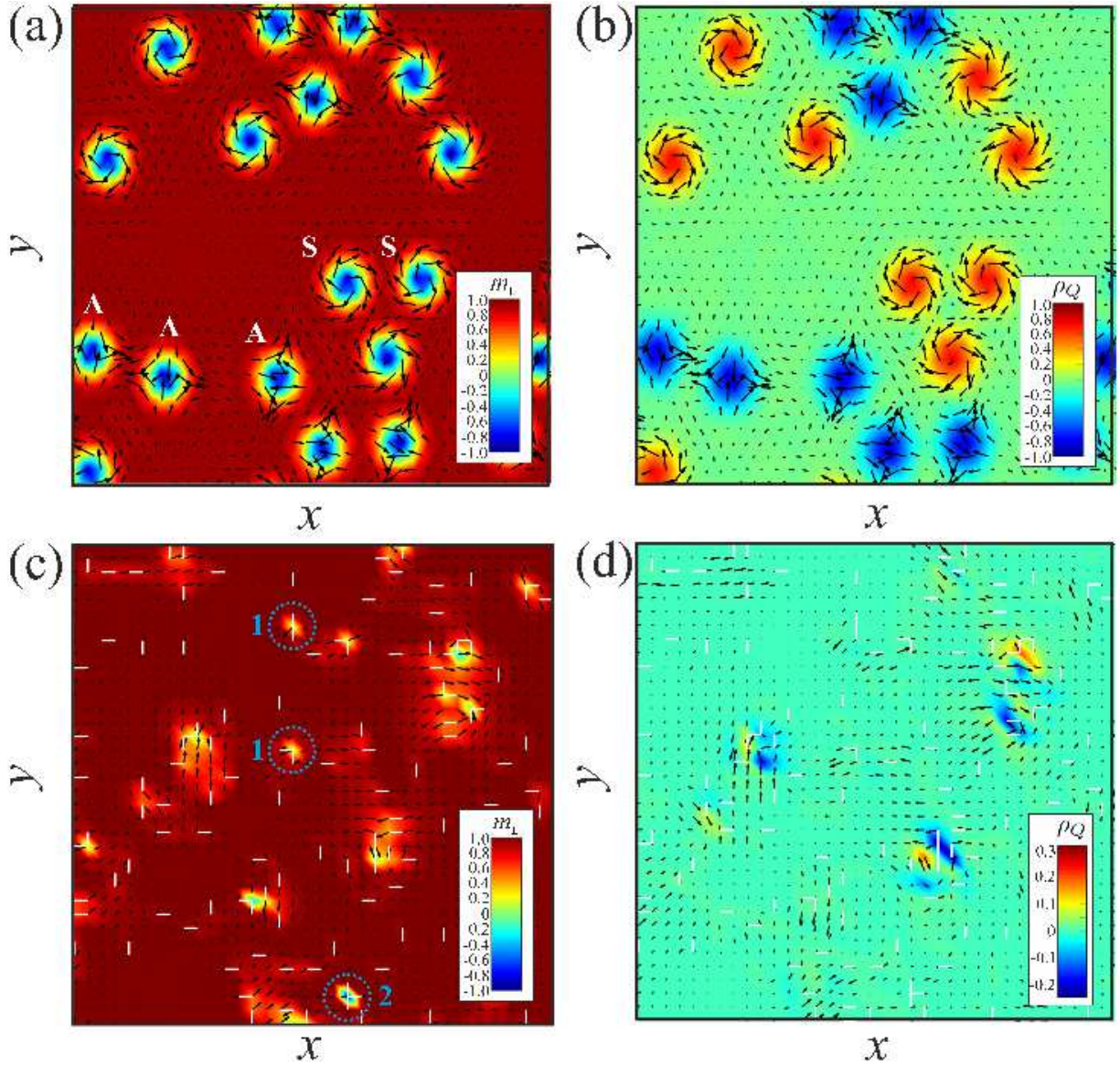


FIG. 7: (a), (b) Skyrmions (S) and antiskyrmions (A) in a frustrated ferromagnet with competing NN and NNN exchange interactions J_1 and J_2 under a field h , with $J_2/J_1 = 0.5$, $h = 0.4$. Typical metastable states featuring clusters of skyrmions and antiskyrmions are obtained by relaxing the magnetic configuration with a random initial spin configuration. Color plots of m_L -components (a) and the topological charge density ρ_Q (b) reflect the smooth rotation of the magnetization within the skyrmion cores. (c), (d) Vortex-like defects induced by interaction disorder as described by a model with random interaction J_{ij} between i, j sites under a field h . The J_{ij} are independent random variables taking the values $+1$ and -1 with probabilities $1 - c$ and c respectively, with $c = 0.05$ and $h = 0.09$. Color plots of m_L -components (c) exhibit various types of spatially localized objects with the balanced topological charge density (d). Blue numbered circles show vortices residing on two or three AFM bonds with distinct magnetization distributions. See Ref. 48 for details.

is field-cooled^{48,65}. However they play a minor role in the stabilization of the vortex state, as exemplified by the MC results which describe a bare Heisenberg system. Experimentally we point out that across the critical concentration, the vortices disappear in the true spin glass phase, while the DM anisotropy hardly changes⁶⁶.

The dissimilarities between vortices and frustrated SKs are more subtle but can be understood by a comparative analysis of their internal structure and topological

charge, as deduced from MC simulations. This comparison is made in details in Ref. 48, and its main results are shown in Fig. 7. Essentially, frustrated SKs are predicted in *ordered* anisotropic magnets with competing interactions and inversion symmetry and do not require antisymmetric exchange²⁹⁻³¹. Their center correspond to a magnetic moment \mathbf{m} antiparallel to the applied field ($m_L < 0$), which gradually rotates towards the aligned state at the boundary ($m_L > 0$). Therefore, they indi-

vidually possess a large topological charge (+1 or -1) and can form densely packed clusters. These features contrast with the vortex-like textures studied in this work, pinned by locally disordered AFM bonds and unable to form extended ordered phases. Since m_L can alternate in sign in the vortex core (as controlled by their internal bond structure), the vortices neither bear smooth rotation of \mathbf{m} nor select a preferred helicity, and their absolute topological charge density is smaller than unity within isolated defects.

Although they cannot form ordered phases, the vortices studied in the present work may form a liquid-like order in the limit of small applied magnetic fields and large concentration of AFM bonds. Finally, both vortices and frustrated SKs remain metastable solutions, found at zero or finite temperatures. They are both endowed with a remarkable robustness against the collapse towards the field-induced FM state and do not require well-defined lattice structures to appear.

V. OUTLOOK AND CONCLUSION

Our study suggests that in the general search for SK-hosting systems, the role of disorder should be investigated more intensively. Its main consequences are expected in the low energy dynamics, associated with glassy states which occur both in average ordered or disordered media. Theoretically, the glassy behavior is related to metastable states with hierarchical structure in the ground state manifold. It can be analyzed in terms of replica field theory, initially developed for spin glasses⁷, then extended to RSGs⁸, vortex lattices in superconductors (the Bragg glass phases⁶⁷) and very recently to

the skyrmion glass phase³⁶. The example of Co-Zn-Mn alloys³⁷ where SK lattices are observed at 300 K and above, is an interesting playground to study such aspects in detail. There, site inversions should lead to local frustration effects and possibly explain the metastable textures observed experimentally.

Our work constitutes an experimental illustration of the importance of frustration and disorder for the emergence of localized spin textures in condensed matter. We suggest a simple mechanism for tuning their properties (density, size) by different parameters such as the magnetic field, heat treatment or concentration. This could open a promising route towards the engineering of bulk systems with well defined sizes and density ranges, for instance the design of vortices by a controllable distribution of bonds. Moreover, while the observed vortices cannot be moved since they are bound to the Mn-Mn pairs, their interaction with electric currents^{68,69} and spin waves⁷⁰⁻⁷² is non trivial. In both cases, the class of frustrated ferromagnets studied in this paper might offer novel ways to encode complex information into electron and heat pulses.

Acknowledgements

We thank P. Bonville for the SQUID measurements, M. Bonnaud for technical assistance on the D33 spectrometer and S. Gautrot and V. Thevenot for their help in setting the experiment on PAXY. A.O.L. acknowledges JSPS Core-to-Core Program, Advanced Research Networks (Japan) and JSPS Grant-in-Aid for Research Activity Start-up 17H06889, and thanks Ulrike Nitzsche for technical assistance.

* isabelle.mirebeau@cea.fr

¹ K. v. Klitzing, G. Dorda, and M. Pepper, *Phys. Rev. Lett.* **45**, 494 (1980).
² D. J. Thouless, M. Kohmoto, M. P. Nightingale, and M. den Nijs, *Phys. Rev. Lett.* **49**, 405 (1982).
³ A. Fert and I. A. Campbell, *Phys. Rev. Lett.* **21**, 1190 (1968).
⁴ M. N. Baibich, J. M. Broto, A. Fert, F. Nguyen Van Dau, F. Petroff, P. Etienne, G. Creuzet, A. Friederich, and J. Chazelas, *Phys. Rev. Lett.* **61**, 2472 (1988).
⁵ P. Le Doussal and T. Giamarchi, *Phys. Rev. B* **57**, 11356 (1998).
⁶ T. Klein, I. Joumard, S. Blanchard, J. Marcus, R. Cubitt, T. Giamarchi, and P. Le Doussal, *Nature* **413**, 404 (2001).
⁷ D. Sherrington and S. Kirkpatrick, *Phys. Rev. Lett.* **35**, 1792 (1975).
⁸ M. Gabay and G. Toulouse, *Phys. Rev. Lett.* **47**, 201 (1981).
⁹ W. Abdul-Razzaq and J. S. Kouvel, *Journal of Applied Physics* **55**, 1623 (1984).
¹⁰ I. A. Campbell, S. Senoussi, F. Varret, J. Teillet, and A. Hamzić, *Phys. Rev. Lett.* **50**, 1615 (1983).

¹¹ K. Motoya, S. M. Shapiro, and Y. Muraoka, *Phys. Rev. B* **28**, 6183 (1983).
¹² P. Böni, S. Shapiro, and K. Motoya, *Solid State Communications* **60**, 881 (1986).
¹³ S. K. Burke and B. D. Rainford, *J. of Physics F: Met. Phys.* **13**, 441 (1983).
¹⁴ M. B. Salamon, K. V. Rao, and H. S. Chen, *Phys. Rev. Lett.* **44**, 596 (1980).
¹⁵ R. J. Birgeneau, J. A. Tarvin, G. Shirane, E. M. Gyorgy, R. C. Sherwood, H. S. Chen, and C. L. Chien, *Phys. Rev. B* **18**, 2192 (1978).
¹⁶ J. A. Fernandez-Baca, J. J. Rhyne, G. E. Fish, M. Hennen, and B. Hennen, *J. Applied Physics* **67**, 5223 (1990).
¹⁷ S. Senoussi, S. Hadjoudj, P. Jouret, J. Bilotte, and R. Fourmeaux, *Journal of Applied Physics* **63**, 4086 (1988).
¹⁸ Senoussi, S., Hadjoudj, S., Fourmeaux, R., and Jaouen, C., *J. Phys. Colloques* **49**, C8 (1988).
¹⁹ M. Hennen, I. Mirebeau, B. Hennen, S. Lequien, and F. Hippert, *EPL (Europhysics Letters)* **2**, 393 (1986).
²⁰ S. Lequien, I. Mirebeau, M. Hennen, B. Hennen, F. Hippert, and A. P. Murani, *Phys. Rev. B* **35**, 7279 (1987).
²¹ M. Hennen, B. Hennen, I. Mirebeau, S. Lequien, and

- F. Hippert, *Journal of Applied Physics* **63**, 4071 (1988).
- ²² I. A. Campbell, H. Hurdequint, and F. Hippert, *Phys. Rev. B* **33**, 3540 (1986).
- ²³ G. Tatara and H. Kawamura, *Journal of the Physical Society of Japan* **71**, 2613 (2002).
- ²⁴ P. Pureur, F. W. Fabris, J. Schaf, and I. A. Campbell, *EPL (Europhysics Letters)* **67**, 123 (2004).
- ²⁵ F. W. Fabris, P. Pureur, J. Schaf, V. N. Vieira, and I. A. Campbell, *Phys. Rev. B* **74**, 214201 (2006).
- ²⁶ H. Kawamura and M. Tanemura, *Journal of the Physical Society of Japan* **60**, 1092 (1991).
- ²⁷ A. Fert, V. Cros, and J. Sampaio, *Nat Nano* **8**, 152 (2013).
- ²⁸ N. Nagaosa and Y. Tokura, *Nature Nano.* **8** (2013).
- ²⁹ T. Okubo, S. Chung, and H. Kawamura, *Phys. Rev. Lett.* **108**, 017206 (2012).
- ³⁰ A. O. Leonov and M. Mostovoy, *Nature Communications* **6**, 8275 (2015).
- ³¹ S.-Z. Lin and S. Hayami, *Phys. Rev. B* **93**, 064430 (2016).
- ³² L. Rózsa, A. Deák, E. Simon, R. Yanes, L. Udvardi, L. Szunyogh, and U. Nowak, *Phys. Rev. Lett.* **117**, 157205 (2016).
- ³³ Y. Hu, X. Chi, X. Li, Y. Liu, and A. Du, *Scientific Reports* **7**, 16079 (2017).
- ³⁴ A. O. Leonov, T. L. Monchesky, N. Romming, A. Kubetzka, A. N. Bogdanov, and W. R., *New J. of Phys.* **18**, 06503 (2016).
- ³⁵ A. O. Leonov, Y. Togawa, T. L. Monchesky, A. N. Bogdanov, J. Kishine, Y. Kousaka, M. Miyagawa, T. Koyama, J. Akimitsu, T. Koyama, et al., *Phys. Rev. Lett.* **117**, 087202 (2016).
- ³⁶ S. Hoshino and N. Nagaosa, *Phys. Rev. B* **97**, 024413 (2018).
- ³⁷ Y. Tokunaga, X. Z. Yu, J. S. White, H. M. Rønnow, D. Morikawa, Y. Taguchi, and Y. Tokura, *Nature Communications* **6**, 7638 (2015).
- ³⁸ A. K. Nayak, V. Kumar, T. Ma, P. Werner, E. Pippel, R. Sahoo, F. Damay, U. K. Röbber, C. Felser, and S. S. P. Parkin, *Nature* **548**, 561 (2017).
- ³⁹ T. Kurumaji, T. Nakajima, M. Hirschberger, A. Kikkawa, Y. Yamasaki, H. Sagayama, H. Nakao, Y. Taguchi, T. Arima, and Y. Tokura, arXiv:1805.10719 (2018).
- ⁴⁰ R. Sommer, J. Schmidt, and A. Gomes, *Journal of Magnetism and Magnetic Materials* **103**, 25 (1992).
- ⁴¹ W. Abdul-Razzaq and J. S. Kouvel, *Phys. Rev. B* **35**, 1764 (1987).
- ⁴² I. Mirebeau, Ph.D. thesis, Université de Paris-Sud (1987).
- ⁴³ M. J. Marcinkowski and N. Brown, *Journal of Applied Physics* **32**, 375 (1961).
- ⁴⁴ J. W. Cable and H. R. Child, *Phys. Rev. B* **10**, 4607 (1974).
- ⁴⁵ Y. Yokoyama and T. Satoh, *Journal of Magnetism and Magnetic Materials* **3**, 347 (1976).
- ⁴⁶ T. Okazaki, *Japanese Journal of Applied Physics* **34**, 1537 (1995).
- ⁴⁷ G. J. Stanisz, J. Soltys, and J. M. Holender, *Journal of Physics: Condensed Matter* **1**, 6327 (1989).
- ⁴⁸ See Supplemental Material at [url] for details about data treatment, calculations of neutron scattering cross sections, additional SANS data, mean-field modeling of the NiMn alloy and a comparative analysis of the structure of vortex-like defects and frustrated skyrmions.
- ⁴⁹ J. W. Lynn, N. Rosov, T. E. Grigereit, H. Zhang, and T. W. Clinton, *Phys. Rev. Lett.* **72**, 3413 (1994).
- ⁵⁰ S. Mühlbauer, B. Binz, F. Jonietz, C. Pfleiderer, A. Rosch, A. Neubauer, R. Georgii, and P. Böni, *Science* **323**, 915 (2009).
- ⁵¹ M. Hennion, D. Ronzaud, and P. Guyot, *Acta Metallurgica* **30**, 599 (1982).
- ⁵² H. Kawamura and M. Tanemura, *Journal of the Physical Society of Japan* **55**, 1802 (1986).
- ⁵³ G. T. Rado, *Phys. Rev. B* **26**, 295 (1982).
- ⁵⁴ M. Steiner, *Journal of Magnetism and Magnetic Materials* **31-34**, 1277 (1983).
- ⁵⁵ J. M. Kosterlitz and D. J. Thouless, *Journal of Physics C: Solid State Physics* **6**, 1181 (1973).
- ⁵⁶ J. M. Kosterlitz, *Rev. Mod. Phys.* **89**, 040501 (2017).
- ⁵⁷ J. Villain (2017).
- ⁵⁸ J. L. Black and B. I. Halperin, *Phys. Rev. B* **16**, 2879 (1977).
- ⁵⁹ K. H. Michel, *Phys. Rev. B* **35**, 1414 (1987).
- ⁶⁰ D. N. Aristov and S. V. Maleyev, *Zeitschrift für Physik B Condensed Matter* **81**, 433 (1990).
- ⁶¹ Toulouse, G. and Kléman, M., *J. Physique Lett.* **37**, 149 (1976).
- ⁶² C. M. Soukoulis, G. S. Grest, and K. Levin, *Phys. Rev. Lett.* **50**, 80 (1983).
- ⁶³ M. J. P. Gingras, *Competition Between Ferromagnetic and Spin Glass Order in Random Magnets: The Problem of Reentrant Spin Glasses* (World Scientific, 1994), pp. 238–285.
- ⁶⁴ S. Senoussi, *Phys. Rev. Lett.* **51**, 2218 (1983).
- ⁶⁵ I. Mirebeau, M. Hennion, S. Lequien, and F. Hippert, *Journal of Applied Physics* **63**, 4077 (1988).
- ⁶⁶ N. Martin, I. Mirebeau *et al.*, in preparation (2018).
- ⁶⁷ T. Giamarchi and P. Le Doussal, *Phys. Rev. B* **52**, 1242 (1995).
- ⁶⁸ D. Prychynenko, M. Sitte, K. Litzius, B. Krüger, G. Bourianoff, M. Kläui, J. Sinova, and K. Everschor-Sitte, *Phys. Rev. Applied* **9**, 014034 (2018).
- ⁶⁹ G. Bourianoff, D. Pinna, M. Sitte, and K. Everschor-Sitte, *AIP Advances* **8**, 055602 (2018).
- ⁷⁰ M. Continentino, *Journal of Magnetism and Magnetic Materials* **31-34**, 1413 (1983).
- ⁷¹ I. Y. Korenblit, S. V. Maleev, and E. F. Shender, *Phys. Rev. B* **33**, 624 (1986).
- ⁷² E. F. Shender and R. Rammal, *EPL (Europhysics Letters)* **15**, 795 (1991).
- ⁷³ A. Brûlet, D. Lairez, A. Lapp, and J.-P. Cotton, *Journal of Applied Crystallography* **40**, 165 (2007).
- ⁷⁴ A.-J. Dianoux and G. Lander, eds., *ILL Neutron Data Booklet* (2003).
- ⁷⁵ C. Dewhurst, *Measurement Science and Technology* **19**, 034007 (2008).
- ⁷⁶ <http://www-llb.cea.fr/spectros/pdf/paxy-llb.pdf>.
- ⁷⁷ K. L. Metlov and A. Michels, *Scientific Reports* **6**, 25055 (2016).
- ⁷⁸ K. A. Ziq and J. S. Kouvel, *Phys. Rev. B* **41**, 4579 (1990).
- ⁷⁹ G. H. Derrick, *Journal of Mathematical Physics* **5**, 1252 (1964).
- ⁸⁰ T. Skyrme, *Nuclear Physics* **31**, 556 (1962).
- ⁸¹ E. Chudnovsky and D. Garanin, arXiv:1710.10608 (2017).

Supplementary material

In this supplement, we provide information about the Small-Angle Neutron Scattering (SANS) data analysis (Section A) and calculations of model form factors of spin vortices as seen by SANS (Section B). In Section C, we give a brief review of the effects of temperature and cooling field on the observed SANS patterns. Mean-field modeling (Section D), relevant to our weakly frustrated $\text{Ni}_{0.81}\text{Mn}_{0.19}$ sample, is also exposed. Finally, an extended comparative analysis of the internal structure of the vortex-like defects evidenced in this work and that of frustrated skyrmions is presented (Section E).

Appendix A: Neutron scattering data analysis

Small-Angle Neutron Scattering (SANS) data has been treated following the usual strategy⁷³, which we briefly summarize here. In a first step, we have to eliminate the extrinsic background arising from direct beam tail and sample environment. This is done by measuring the raw intensity $I_{\text{empty holder}}^{\text{raw}}$ obtained with the empty sample holder placed at the sample position. The latter is then subtracted from the scattering pattern to be analyzed, yielding

$$I_i^{\text{corr}} = I_i^{\text{raw}} - t_i \cdot I_{\text{empty holder}}^{\text{raw}} \quad , \quad (\text{A1})$$

where i denotes the studied sample ($\text{Ni}_{0.81}\text{Mn}_{0.19}$) or a calibrant (in the present case, a single crystal of pure Ni). Then, scattered intensities can be converted to cross sections *on an absolute scale* using the expression

$$\sigma_{\text{NiMn}}(q) = \frac{I_{\text{NiMn}}^{\text{corr}} \cdot t_{\text{Ni}} \cdot d_{\text{Ni}} \cdot e_{\text{Ni}}}{\langle I_{\text{Ni}}^{\text{corr}}(q) \rangle \cdot t_{\text{NiMn}} \cdot d_{\text{NiMn}} \cdot e_{\text{NiMn}}} \cdot \sigma_{\text{Ni}}^{\text{inc}} \quad , \quad (\text{A2})$$

where t , d and e denote transmissions, atomic densities and thicknesses, respectively, while $\sigma_{\text{Ni}}^{\text{inc}} = \frac{5.2}{4\pi}$ barn \cdot sr $^{-1}$ is the incoherent scattering cross section of Ni (taken from Ref. 74).

As shown by the results presented in Fig. 4 of main text, this strategy allows obtaining cross sections which

agree to within a few % between the experiments performed on two different SANS spectrometers (D33 at Institut Laue Langevin⁷⁵ and PAXY at Laboratoire Léon Brillouin⁷⁶).

To determine the longitudinal and transverse cross sections, we use the configuration b) where the magnetic field \mathbf{H} is in the detector plane and α is the angle (\mathbf{q}, \mathbf{H}). We average the scattering map within two angular sectors of 60° : sector 1 for $\alpha = 0$ ($\mathbf{q} // \mathbf{H}$) and sector 2 for $\alpha = \pi/2$ ($\mathbf{q} \perp \mathbf{H}$) (see Figs. 2 and 3 of main text). Then we combine the intensities of the two sectors to deduce $\sigma_{\text{T}}(q)$ and $\sigma_{\text{L}}(q)$. The intensities write:

$$\sigma_{\text{T}}(q) + I_{\text{bg}}(q)/2 = \sigma(\mathbf{q}, 0)/2 \quad (\text{A3a})$$

$$\sigma_{\text{L}}(q) + I_{\text{bg}}(q)/2 = \sigma(\mathbf{q}, \pi/2) - \sigma(\mathbf{q}, 0)/2 \quad (\text{A3b})$$

In a second step we discuss the origin of the intrinsic background term $I_{\text{bg}}(q)$, which must be evaluated to isolate the vortex cross sections $\sigma_{\text{T}}(q)$ and $\sigma_{\text{L}}(q)$. This background term originates from the sample itself and is quasi-isotropic in the detector plane. It is well accounted by the expression:

$$I_{\text{bg}}(q) = \frac{a}{q^p} + b \quad . \quad (\text{A4})$$

The first term $\frac{a}{q^p}$ dominates in the low- q region ($q \leq 0.025 \text{\AA}^{-1}$) and strongly increases down to $q \rightarrow 0$ following a power law. This small-angle scattering originates from long range nuclear and magnetic inhomogeneities, such as crystal dislocations or magnetic domain walls. The nuclear part could be estimated in principle by performing measurements at a very large fields when the whole magnetic contribution is negligible, but the magnetic part is always present and introduces a slight anisotropy in the background intensity. By fitting the low- q tail, we find a power-law exponent $p = 3.2$ in all cases. This value has been fixed in the course of data evaluation.

The second term of Eq. A4 is a q -independent contribution arising from incoherent scattering and chemical disorder (namely the Laue scattering) in the sample. It can be calculated exactly, knowing the amount of chemical short range order. This term is expressed as:

$$b = \underbrace{(1-x) \cdot \sigma_{\text{Ni}}^{\text{inc}} + x \cdot \sigma_{\text{Mn}}^{\text{inc}}}_{\text{Incoherent scattering}} + x \cdot (1-x) \cdot \underbrace{\left(1 + \sum_{i=1}^3 z_i \alpha(R_i)\right)}_{\text{Disorder scattering}} \cdot (b_{\text{Ni}}^{\text{coh}} - b_{\text{Mn}}^{\text{coh}})^2 \quad , \quad (\text{A5})$$

where x is the atomic concentration of Mn, $\sigma_{\text{Ni},\text{Mn}}^{\text{inc}}$ the incoherent scattering cross sections of Ni and Mn, $b_{\text{Ni},\text{Mn}}^{\text{coh}}$

the coherent scattering lengths of Ni and Mn, z_i the number of i^{th} neighbors in the face-centered cubic structure

and $\alpha(R_i)$ the corresponding positional short-range order parameters obtained on $\text{Ni}_{0.8}\text{Mn}_{0.2}^1$ by Cable and Child⁴⁴ (see Tab. I). Taken together, we obtain $b = 590$ mbarn. This yields a background level of $b/2 = 295$ mbarn for σ_L and σ_T , in *quantitative* agreement with the experiment (see Fig. 8, and Figs. 3e and 4a,b of main text). This excellent accordance shows that the corrections of environmental background and the calibration of the data in absolute scale are truly reliable.

TABLE I: Positional short-range order parameters of $\text{Ni}_{0.8}\text{Mn}_{0.2}$, from Ref. 44.

	z	$\alpha(R)$
1 st neighbors	12	-0.09
2 nd neighbors	6	+0.07
3 rd neighbors	24	+0.02

In summary, to account for the intrinsic background, we can either refine by fitting Eq. A4 to the data with the parameters p and b being fixed, or account for it by subtracting a pattern at the highest measured field of 8 T. In Fig. 8 below, we compare the longitudinal and transverse cross sections with and without subtraction. The high field subtraction singles out the magnetic contribution from the vortices. However it is not very accurate at low q (*i.e.* at $q \leq 0.025 \text{\AA}^{-1}$, see pink area in Fig. 8), especially for the longitudinal cross section, and it neglects the vortex contribution at 8 T, which can still be detected. This is why we have chosen the fitting procedure and we present the non subtracted data in the main text. We emphasize that the qualitative conclusions reached in the main text are unaffected by the choice of data treatment method.

Appendix B: Analytical expressions for the form factor of a spin vortex

In order to support the results presented in main text, we carry out calculations of a spin vortex form factor

as seen by SANS. We assume a regular vortex of radius R , in a field $H//x$ (see Fig.9). $m_L(r)$ and $m_T(r)$ are the components of the local moment along the field and perpendicular to it, respectively called longitudinal and transverse. Analytical expressions for the longitudinal F_L and transverse F_T form factors are obtained using `Wolfram Mathematica 10.4`.

We start by defining the spin field that we use to model a regular vortex in the cartesian frame of Fig. 9:

$$\mathbf{m} = \begin{pmatrix} m_L(r) \\ m_T(r) \cdot \cos(\psi + \delta) \\ m_T(r) \cdot \sin(\psi + \delta) \end{pmatrix}, \quad (\text{B1})$$

where r and ψ are polar coordinates in the (y, z) -plane and δ the angle formed by individual spins with respect to the concentric vortex lines. The corresponding structure factors are obtained by Fourier transforming Eq. B1:

$$F_i = \frac{1}{\pi} \int_{-\pi}^{\pi} \left(\frac{1}{2\pi R^2} \int_{-\pi}^{\pi} \int_0^R m_i e^{iqr} r dr d\psi \right) d\delta, \quad (\text{B2})$$

where $i = \{x, y, z\}$. As expressed by Eq. 4 of the main text, the magnetic neutron scattering cross section explicitly contains $\langle F_i \rangle^2$ and $\langle F_i^2 \rangle$. First neglecting a possible r -dependence of m_L and m_T , symmetry considerations² lead to:

$$\langle F_x^2(q) \rangle = \langle F_x(q) \rangle^2 = \left(\frac{m_L}{2\pi R^2} \int_0^R \int_{-\pi}^{\pi} r \cos(qr) dr d\psi \right)^2 = \left(\frac{2m_L}{qR} \right)^2 \cdot J_1^2(qR), \quad (\text{B3})$$

$$\begin{aligned}
\langle F_y^2(q) \rangle &= \frac{1}{\pi} \cdot \int_{-\pi}^{\pi} \left(\frac{m_T}{2\pi R^2} \int_0^R \int_{-\pi}^{\pi} \cos(\psi + \delta) r \sin(qr) dr d\psi \right)^2 d\delta \\
&= \frac{1}{\pi} \cdot \int_{-\pi}^{\pi} \frac{\pi^2 m_T^2 \cdot (J_1(qR) \cdot H_0(qR) - J_0(qR) \cdot H_1(qR))^2 \cdot \cos^2 \delta}{4q^2 R^2} d\delta \\
&= \frac{\pi^2 m_T^2 \cdot (J_1(qR) \cdot H_0(qR) - J_0(qR) \cdot H_1(qR))^2}{4q^2 R^2} ;
\end{aligned} \tag{B4}$$

$$\langle F_y(q) \rangle^2 = 0 ,$$

$$\begin{aligned}
\langle F_z^2(q) \rangle &= \frac{1}{\pi} \cdot \int_{-\pi}^{\pi} \left(\frac{m_T}{2\pi R^2} \int_0^R \int_{-\pi}^{\pi} \sin(\psi + \delta) r \sin(qr) dr d\psi \right)^2 d\delta \\
&= \frac{1}{\pi} \cdot \int_{-\pi}^{\pi} \frac{\pi^2 m_T^2 \cdot (J_1(qR) \cdot H_0(qR) - J_0(qR) \cdot H_1(qR))^2 \cdot \sin^2 \delta}{4q^2 R^2} d\delta \\
&= \frac{\pi^2 m_T^2 \cdot (J_1(qR) \cdot H_0(qR) - J_0(qR) \cdot H_1(qR))^2}{4q^2 R^2} ;
\end{aligned} \tag{B5}$$

$$\langle F_z(q) \rangle^2 = 0 ,$$

where J_n (H_n) are Bessel (Struve) functions of order n . We note that Eqs. B3, B4 and B5 are equivalent to the results obtained by Metlov and Michels for a centered vortex in a ferromagnetic nanodot (see Eq. 13 from Ref. 77).

The average squared form factor $\langle F_y^2(q) \rangle = \langle F_z^2(q) \rangle$ shows a maximum vs. q (Fig. 10), as expected since the transverse spin components compensate within the vortex, yielding zero intensity at $q=0$. However, in the context of a bulk disordered ferromagnet, we cannot physically consider constant transverse magnetization since it would imply a sudden jump to $m_T = 0$ outside of the

vortex, *i.e.* in the average ferromagnetic medium. If we assume instead that $m_T(r)$ is maximum at the vortex center ($r = 0$) and continuously decreases away from the center as $m_T(r) = m_T \cdot (1 - r/R)$ (see Fig. 9), this choice restores continuity at the vortex edge. This average description neglects the local variations of the moments orientations such as those induced by different Mn and Ni moments, or by an AF core constituted of first neighbor Mn-Mn pairs, which would yield smooth modulations of the diffuse scattering at larger q -values. With these assumptions, the transverse form factors are now expressed as:

$$\begin{aligned}
\langle F_y^2(q) \rangle &= \langle F_z^2(q) \rangle \\
&= \frac{m_T^2 \cdot [J_1(qR) \cdot (\pi q R H_0(qR) - 4) + q R J_0(qR) \cdot (2 - \pi H_1(qR))]^2}{q^4 R^6} ;
\end{aligned} \tag{B6}$$

$$\langle F_y(q) \rangle^2 = \langle F_z(q) \rangle^2 = 0 .$$

As shown in Fig. 10, Eqs. B4-B5 and Eq. B6 both yield peaks in the transverse form factors, but at different q values. The peak positions q_{\max} differ appreciably but have a $1/r_d$ -dependence in common: $q_{\max} \simeq 0.78 \pi/r_d$ in the former case, $q_{\max} \simeq \pi/r_d$ in the latter case (see Fig. 10a). As explained above, the second model seems closer to reality for continuity reasons. This motivated

our choice to relate the defect size to π/q_{\max} (see main text). Eq. B6 also yields more asymmetric peaks, in closer proximity to the experimental transverse cross sections (see Fig. 10b and compare with Fig. 3e of main text). The variation of $m_T(r)$ should be accompanied with a correlated variation of $m_L(r)$ with respect to the average magnetization, which is likely too small to be

observed (see main text).

Appendix C: Effect of temperature and cooling-field on the SANS patterns

While the work presented in main text is focused on the low temperature properties of the defects studied by small-angle neutron scattering and their relation to the ground state properties of $\text{Ni}_{0.81}\text{Mn}_{0.19}$, we provide here some details about the temperature- and cooling-field dependence of the experimental patterns.

As shown in Fig. 11a-c, increasing temperature leads to the progressive rise of the small-angle intensity and a concomitant vanishing of the peak feature in the observed cross section, already well-below the canting temperature $T_K \sim 120$ K. This is due to the thermal activation of spin waves, which contribute to the scattered intensity since inelastic processes are not filtered out in a SANS setup. This leads to a non-trivial evolution of the total intensity, which strongly depends on the applied magnetic field (see Fig. 11d). It has been shown in Ref. 20 (using a three-axis spectrometer which allows isolating purely elastic scattering at the expense of neutron flux) that the signal associated with vortex-like defects vanishes only at T_K while the vortex size remains basically constant as a function of temperature, in agreement with theoretical expectations. Altogether, this justifies our experimental strategy which concentrates on the low-temperature regime, where the properties of the field-induced "croustons" can be conveniently studied and compared to "T = 0" MC simulations.

On the other hand, in the $\text{Ni}_{0.81}\text{Mn}_{0.19}$ sample which behaves as a "rigid" system, the application of a magnetic field H_{cool} upon cooling reveals the existence of unidirectional anisotropy induced by Dzyaloshinskii-Moryia interactions, the cooling field acting as an additional bias field⁷⁸. Our SANS study reveals that the transverse correlations are substantially modified by H_{cool} , although the bare plateau magnetization is basically not affected⁶⁵. Indeed, SANS patterns recorded for different values of H_{cool} at low temperature clearly display different peak positions and intensities (see Fig. 12a). Essentially, increasing H_{cool} favors smaller defects at equal applied field value. The scaling laws which govern the evolution of the defect size are however preserved, as shown in Fig. 12b where the law $q_{\text{max}} \propto \mu_0 H_{\text{int}}^{1/2}$ remains valid for all fields (except for applied fields smaller than 1 T for $H_{\text{cool}} = 2$ T). These aspects highlight the importance of the neutron probe to the study of fine magnetic features of RSGs.

Appendix D: Mean-field phase diagram and effective antiferromagnetic bond concentration

The re-entrant spin-glass (RSG) phase has been studied theoretically by many authors. Here, we use the celebrated model of Gabay and Toulouse⁸ to compare the mean-field phase diagram with the experimental one and estimate the effective antiferromagnetic (AFM) bond concentration of our $\text{Ni}_{0.81}\text{Mn}_{0.19}$ sample.

The phase diagram of RSG's (Fig. 13) is calculated in mean field approximation for interactions with infinite range. The spins of the i and j sites interact via independent random interactions J_{ij} , distributed according to a normalized Gaussian law:

$$p(J_{ij}) = \sqrt{\frac{N}{2\pi}} \cdot \exp\left[-\frac{N}{2} \left(J_{ij} - \frac{J_0}{N}\right)^2\right] \quad (\text{D1})$$

where N is the number of sites and J_0 is the average exchange interaction. Namely $\langle J_{ij} \rangle_b = J_0/N$ and $\langle J_{ij}^2 \rangle_b = 1/N$ where $\langle \rangle_b$ denotes an average over bond disorder, that is over $p(J_{ij})$. As shown in Fig. 13, for $J_0 = 0$ and $J_0 \leq 1$, the low temperature phase is a spin glass (SG), showing no long range order. A tricritical point is observed for $J_0 = 1$. In the region $J_0 \geq 1$, long range ferromagnetic order can occur. The system first evolves from paramagnetic (PM) to ferromagnetic (FM) at $T = T_C = J_0$ upon cooling. At lower temperatures, two mixed phases, M1 and M2, are subsequently stabilized, corresponding to the freezing of transverse spin components (M1) and strong irreversibilities in the magnetization (M2). Most importantly, the magnetic LRO is not broken and persists both in M1 and M2 phases. This is the main difference between the RSG and SG's. In the usual terminology, the FM-M1 transition (or Gabay-Toulouse line) takes place at the canting temperature T_K , while the M1-M2 transition (or de Almeida-Thouless line) occurs at the freezing temperature T_F . We have kept these notations in the main text. The transition lines are calculated analytically according to Eqs. 10 and 11 of Ref. 8.

The Gabay-Toulouse model yields a rather accurate description of the experimental phase diagrams of RSG's systems by mapping the average J_0 interaction to the concentration of magnetic species. In $\text{Ni}_{0.81}\text{Mn}_{0.19}$, the characteristic temperatures determined by susceptibility (this work, see Fig. 1 of main text) and neutron scattering (Ref. 20) are $T_C = 257$ K, $T_F = 18$ K and $T_K \simeq 120$ K, yielding a ratio T_F/T_C close to 0.07.

We first determine the appropriate value of J_0 for our compound. In Fig. 13, the ratio $T_F/T_C = 0.07$ corresponds to $J_0 = 1.48$. Using this value, we see that T_K lies below the calculated transition line. The agreement is however satisfactory, considering: i) the simplifying hypothesis made to calculate the mean field diagram; ii) that the determination of T_K is non trivial and the associated error bar ought to be large.

Next, we use the derived value of J_0 to calculate the corresponding probability distribution function (PDF) of random-bond interactions used for MC simulations, assuming a random distribution of AFM bonds (-J) of concentration c in a ferromagnetic medium (J). Integrating the PDF over negative J_{ij} 's, we determine an equivalent AFM bond concentration of $\simeq 7\%$. This justifies the comparison between experiment and MC calculation for a weak concentration of AFM bonds (namely 5 %).

Appendix E: A comparative analysis of internal structure of frustrated skyrmions and vortex-like defects

In the present section, we give a comparative analysis of internal structure of so called "frustrated skyrmions" (see Ref. 30 for further details) and vortex-like defects investigated in the present paper. In both cases, the competing FM and AFM exchange interactions lead to the stability of particle-like states with non-trivial topology but showing different inherent properties.

To stabilize "frustrated skyrmions", we consider the following model with FM nearest-neighbour (NN) and AFM next-nearest-neighbour (NNN) exchange interactions:

$$E = -J_1 \sum_{\langle i,j \rangle} \mathbf{m}_i \cdot \mathbf{m}_j + J_2 \sum_{\langle\langle i,j \rangle\rangle} \mathbf{m}_i \cdot \mathbf{m}_j - h \sum_i m_i^z. \quad (\text{E1})$$

where $\langle i,j \rangle$ and $\langle\langle i,j \rangle\rangle$ denote pairs of NN and NNN spins of unit length, \mathbf{m}_i , respectively, and $J_1, J_2 > 0$. The third term describes the interaction with the magnetic field parallel to z axis. The stability mechanism is provided by the quartic differential terms (in general, by the terms with higher-order derivatives) that appear in the continuum version of Eq. (E1) and allow to overcome the limitations imposed by the Derrick theorem⁷⁹. This mechanism is a reminiscence of the original mechanism of the dynamical stabilization proposed by Skyrme⁸⁰.

In "frustrated skyrmions", the vector \mathbf{m} is antiparallel to z -axis at the center and gradually rotates towards the field-aligned state at the boundary, thus, resulting in circular particle-like states (Fig. 14a,b). The angle between two adjacent spins within the skyrmion cores is controlled by the ratio J_2/J_1 in Eq. (E1) and in the present case ($J_2/J_1 = 0.5$) may reach the value $\pi/3$.

A prominent property of such frustrated magnets with competing exchange interactions is that a skyrmion and an antiskyrmion have the same energy irrespective to their helicity. Skyrmions and antiskyrmions are distinguished conventionally based on the sign of their topological charge being either $+1$ or -1 , correspondingly. The topological charge density, ρ_Q , maintains the same sign within the skyrmion cores (see Fig. 14b with orange and blue coloring used for skyrmions and antiskyrmions, respectively).

With an increasing magnetic field, the skyrmions may undergo the collapse into the homogeneous state. Within the discrete model (E1), the collapse occurs when the negative m_z -component of the magnetization within the skyrmion cores reaches 0; at this point, a skyrmion can be abruptly unwound (see in particular Fig. 6c in Ref. 34 for more details of such a process).

In some range of applied magnetic field, the skyrmions represent metastable states: their energy is higher than the energy of the homogeneously magnetized state. Usually, as shown in Fig. 14a, one observes clusters of such metastable skyrmions and anti-skyrmions with mutual attracting interaction that are embedded into the homogeneously magnetized matrix³⁰. With decreasing magnetic field, the skyrmions tend to crystallize predominantly in a hexagonal lattice with the densest packing of skyrmions: at some critical field ($h < 0.35$ in the model (E1) with the chosen parameters³⁰), the energy of an isolated skyrmion becomes negative with respect to the homogeneous state and hence the skyrmions try to fill the space. The extended skyrmion lattice is determined by the stability of the localized solitonic skyrmion cores and their geometrical incompatibility in the corners of hexagons which frustrates regular space-filling.

However if the formation of a skyrmion lattice is suppressed, isolated skyrmions continue to exist below the critical field. At the same time, isolated skyrmions have a tendency to elongate and expand into a band with helical or cycloidal modulations and eventually to fill the whole space, since the spiral state represents the minimum with lower energy as compared to the local minima with the metastable isolated skyrmions.

Thus, the existence region of "frustrated" skyrmions is restricted by a collapse at high fields and the critical low field at which the energy of an isolated skyrmion becomes negative and thus instigates the formation of the lattice or its elliptical instability³⁴.

The processes of lattice formation or elliptical instability are obviously not the case for vortex-like defects: residing around the AFM bonds, the vortices cannot form any type of an extended ordered phase. However, as pointed out in the main text, with the decreasing magnetic field and an increasing concentration of AFM bonds, the vortices form a liquid-like order stipulated by the same tendency to fill the space although remaining metastable solutions.

Solutions for vortex-like defects induced by interaction disorder are obtained by minimizing the following Hamiltonian:

$$E = - \sum_{\langle i,j \rangle} J_{ij} \mathbf{m}_i \cdot \mathbf{m}_j - h \sum_i m_i^z. \quad (\text{E2})$$

where the sum $\langle i,j \rangle$ runs only over NN pairs. The J_{ij} are independent random variables taking the values $+1$ and -1 with probability $1-c$ and c , correspondingly (see Sec. D). The method used to obtain the vortex configurations

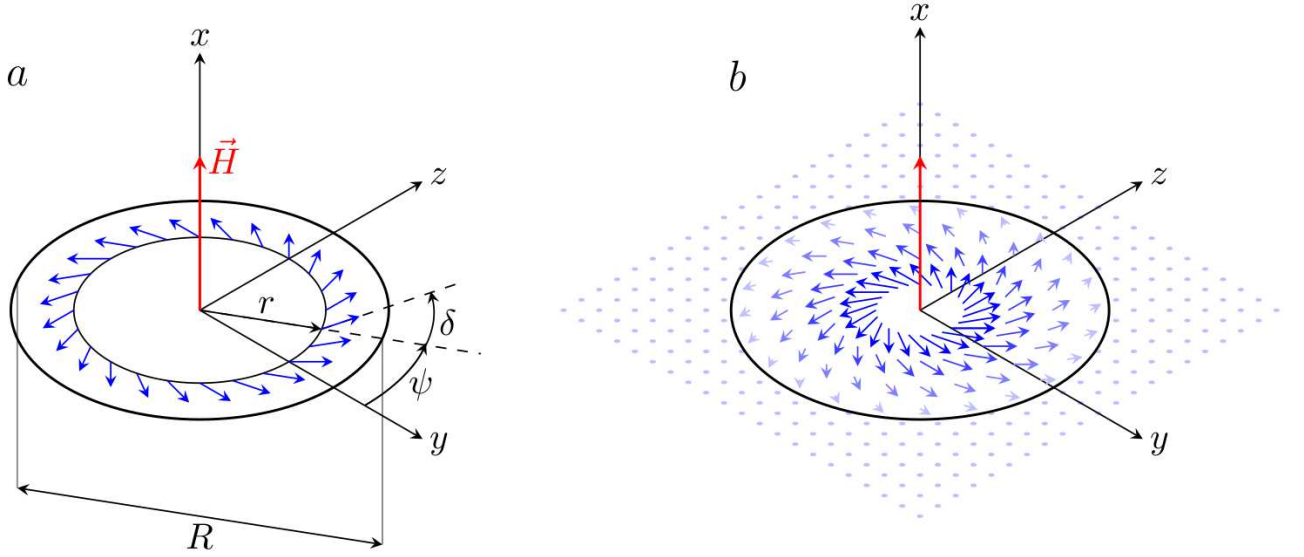
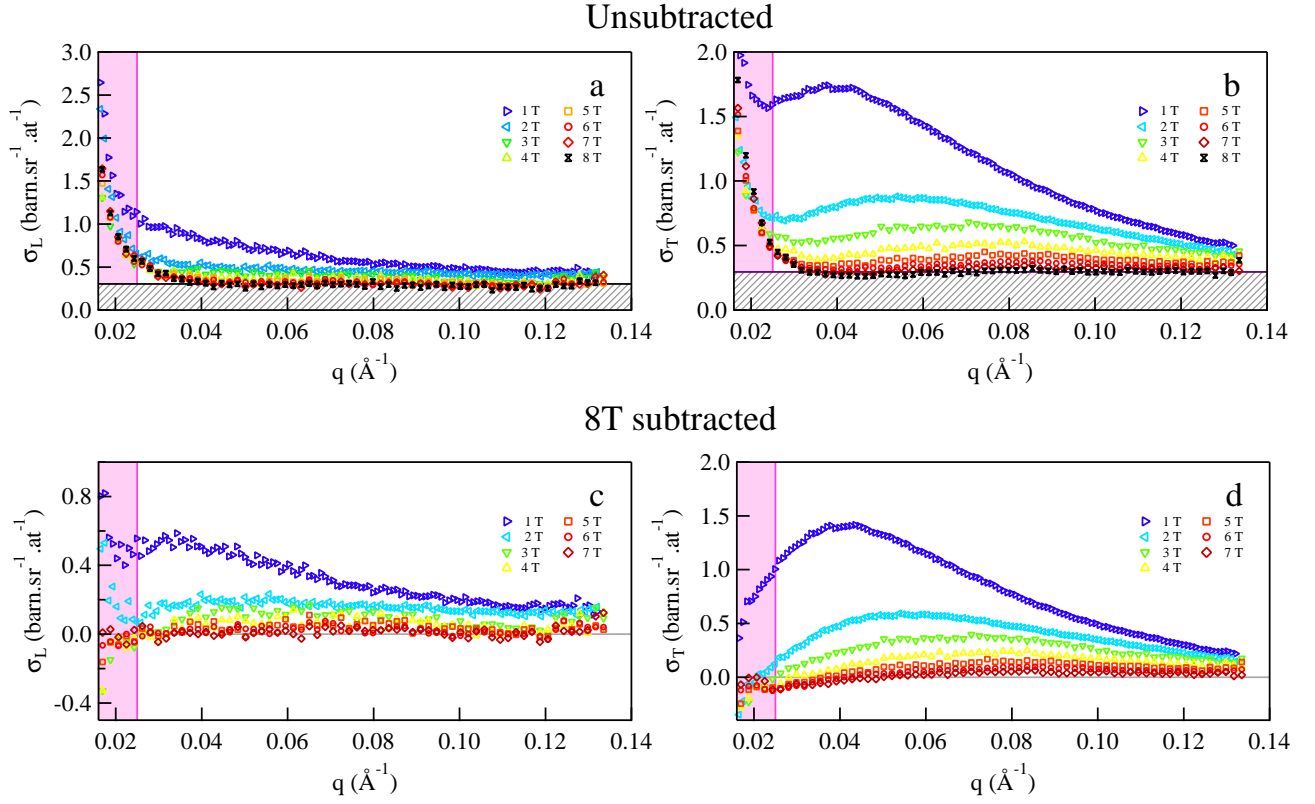
in Fig. 14c,d is described in Ref. 26 and is basically the same as for "frustrated" skyrmions³⁰.

The stabilized vortices are metastable solutions in the whole range of an applied magnetic field. The vortices do not bear any smooth rotation of the magnetization and do not have any preferred helicity. As a consequence, the topological charge density has both signs within one isolated vortex as depicted in Fig. 14d. The largest angle value between two adjacent spins obviously may reach π (see, in particular, a vortex encircled by a blue dotted line and numbered 2 in Fig. 14c). The common case, however, are the spatially localized vortices with the positive m_z -component (which is impossible for frustrated skyrmions) and rather small angles between spins (see vortices numbered 1 in Fig. 14c). Having different number of AFM bonds within the cores, the vortices also exhibit different collapse fields. In particular, for the configuration depicted in Fig. 14c, no vortices rest on single AFM bonds, and vortices on two bonds (blue circles) are close to their transformation into the homogeneous state. Thus, a specified internal structure of a vortex might reflect an exact distribution of AFM bonds in its core or its vicinity, which allows classification of such vortex states with the subsequent engineering of their properties. In particular, an endeavour with creating a smooth magnetization rotation by a particular pattern of AFM bonds could be undertaken. Thus, the existence region of vortex-like defects is restricted by a collapse at high fields (that depends on the internal structure of isolated particles) and the critical low field (and/or concentration c) at which the vortices form a liquid-like state.

Finally, it is instructive to compare the field-dependence of the number of isolated vortex-like defects N_d as obtained by MC simulation with that derived from our small-angle neutron scattering experiment (see Figs. 4f and 6f of main text, and Fig. 15). As explained in main text, a qualitative agreement between calculation

and experiment is observed, namely a global increase of N_d with increasing field, followed by a saturation at a finite field. Remarkably, a fit of a stretched exponential (Eq. 4 of main text) to the data yields similar agreement in the two cases (Fig. 15a,b). This underscores similar evolutions of the defect size and integrated scattering intensity (or square amplitude of the Fourier transform of the transverse magnetization distribution), despite seemingly different local interaction schemes (see main text). However, we point out that the inflection point of the N_d vs. H occurs around $H_C \simeq J$ in the simulation. A mapping to the experimental case suggests that N_d should not cease increasing for fields much smaller than several 100 T in our $\text{Ni}_{0.81}\text{Mn}_{0.19}$ sample, as opposed to our observations. The origin of such disagreement might be due to the willingly simplified approach we have followed to model the distribution of magnetic interactions in the MC simulations. In order to achieve a better control on the properties of systems supporting vortex- or skyrmion-like textures, our work could thus motivate further theoretical work, combining the effects of exchange frustration²⁹⁻³¹ and quenched disorder⁸¹, which have only been considered separately up to now. However, this will not be a simple exercise.

Altogether, our combined experimental and numerical investigation of the properties of the field-induced vortex-like defects stabilized in the $\text{Ni}_{0.81}\text{Mn}_{0.19}$ RSG leads to a simple physical picture. At low magnetic fields (Fig. 15c), the defects are large and encompass several AFM (Mn-Mn) pairs, such that their apparent number N_d is small. Upon field increase, however, their size decrease while they remain fixed around the AFM pairs (Fig. 15d), the number of which being fixed by the Mn concentration and heat treatment. This leads to an increase of N_d . Its value is expected to saturate when defects start collapsing, *i.e.* when spins are locally aligned by the applied field.



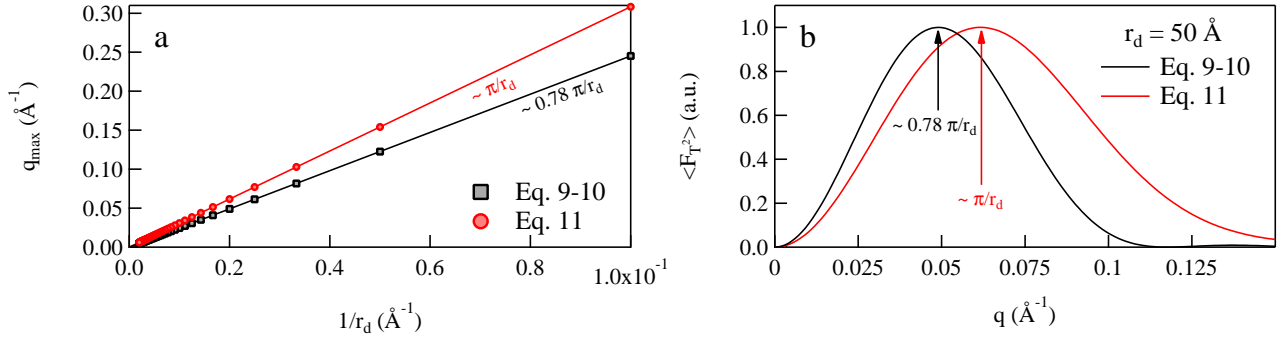


FIG. 10: (a) Evolution of the magnetic scattering peak position as a function of the inverse defect radius for the two models described in text. In both case, the dependences are fully linear, yet with different slopes. (b) Transverse form factors for a vortex of 50 Å radius calculated using Eqs. B4-B5 and Eq. B6, respectively. In the second case, the peak shape is asymmetric, in agreement with the experimental SANS data.

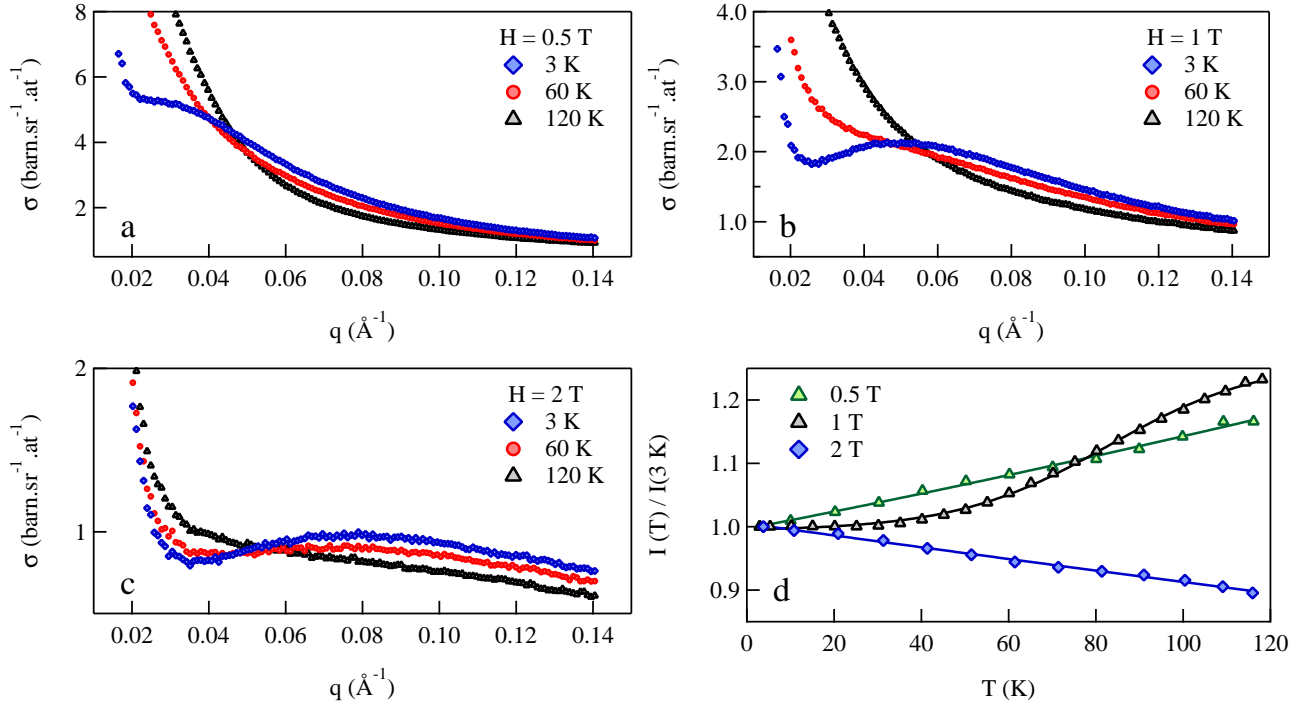


FIG. 11: (a-c) Temperature-dependence of the SANS patterns for applied fields $H = 0.5 \text{ T}$ (a), 1 T (b) and 2 T (c) recorded upon cooling from $T \simeq T_K \sim 120 \text{ K}$. (d) Temperature-dependence of the scattered intensity, integrated over the explored momentum transfer range $0.016 \leq q \leq 0.14 \text{ \AA}^{-1}$ and scaled to its value at $T = 3 \text{ K}$.

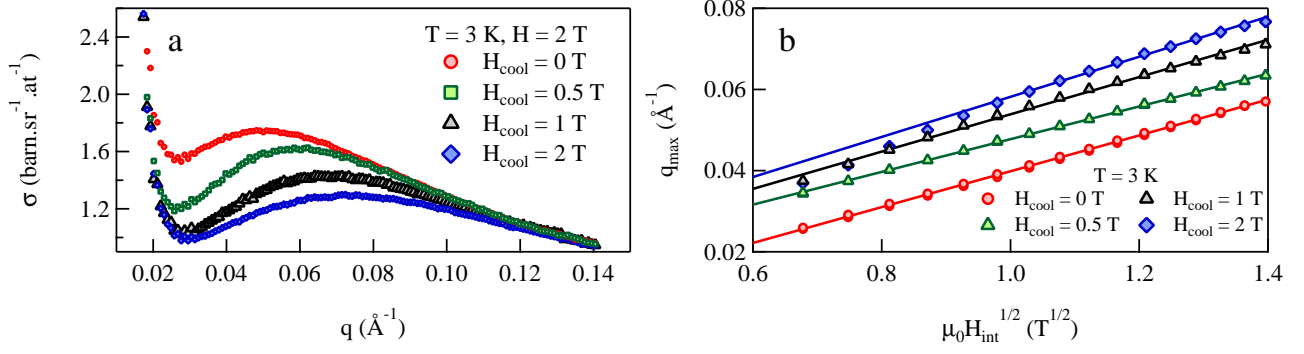


FIG. 12: (a) Influence of a cooling-field H_{cool} on the low temperature SANS patterns, showing a systematic shift and decrease of the peak position and intensity, respectively. (b) Field-dependence of the peak position q_{max} for different values of H_{cool} at $T = 3$ K.

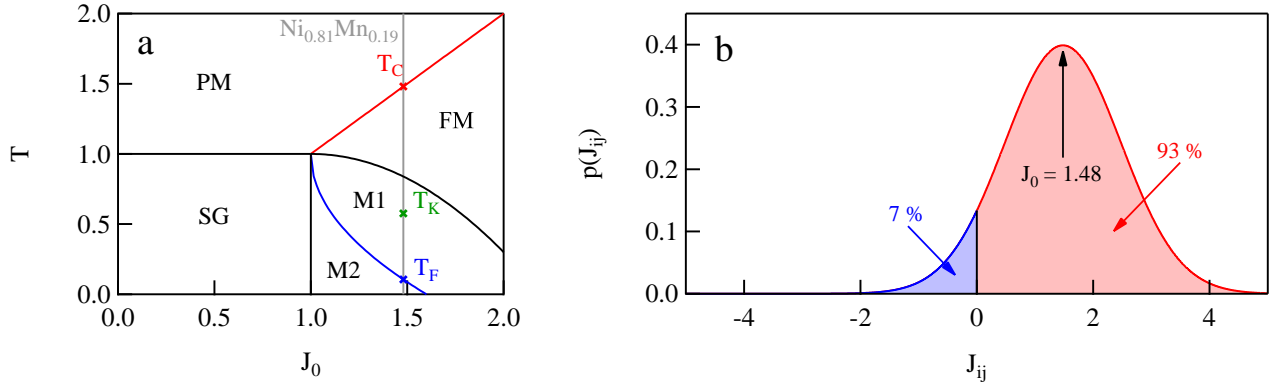


FIG. 13: (a) Mean-field phase diagram of a bond-disordered ferromagnet calculated using the model of Gabay and Toulouse⁸. T_C , T_K and T_F are the experimental Curie, canting and spin freezing temperature of $\text{Ni}_{0.81}\text{Mn}_{0.19}$, respectively. (b) Probability distribution function of the random-bond interactions calculated using Eq. D1 with $J_0 = 1.48$. The blue (red) shaded region correspond to effective AFM (FM) interactions (see text).

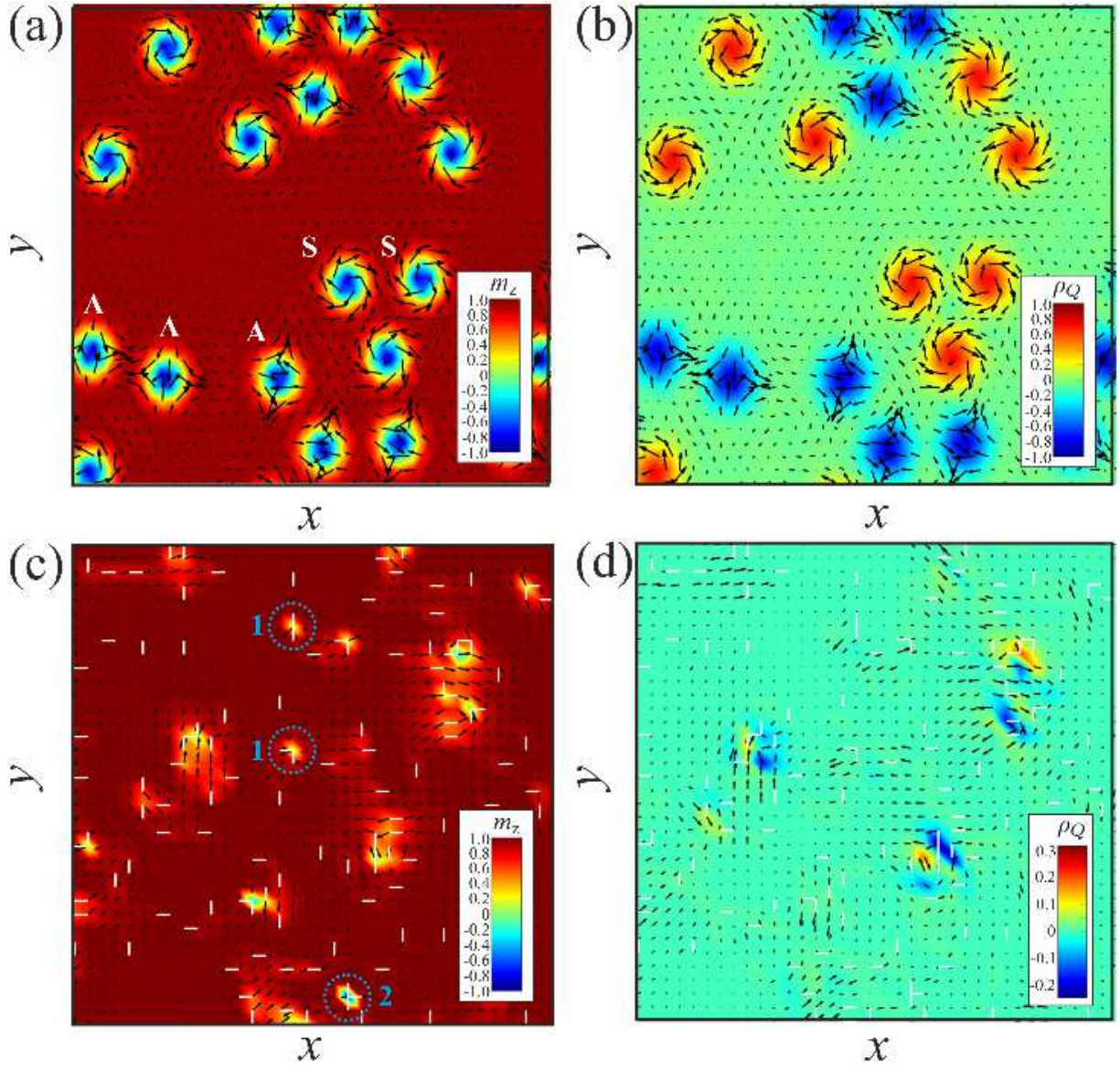


FIG. 14: (a), (b) Skyrmions (S) and antiskyrmions (A) in a frustrated ferromagnet with competing exchange interactions as described by the model (E1) with $J_2/J_1 = 0.5$, $h = 0.4$. Typical metastable states featuring clusters of skyrmions and antiskyrmions are obtained by relaxing the magnetic configuration with a random initial spin configuration. Color plots of m_z -components (a) and the topological charge density ρ_Q (b) reflect the smooth rotation of the magnetization within the skyrmion cores. (c), (d) Vortex-like defects induced by interaction disorder as described by the model (E2) with $c = 0.05$ and $h = 0.09$. Color plots of m_z -components (c) exhibit various types of spatially localized objects with the balanced topological charge density (d). Blue numbered circles show vortices residing on two or three AFM bonds with distinct magnetization distributions (see text for details).

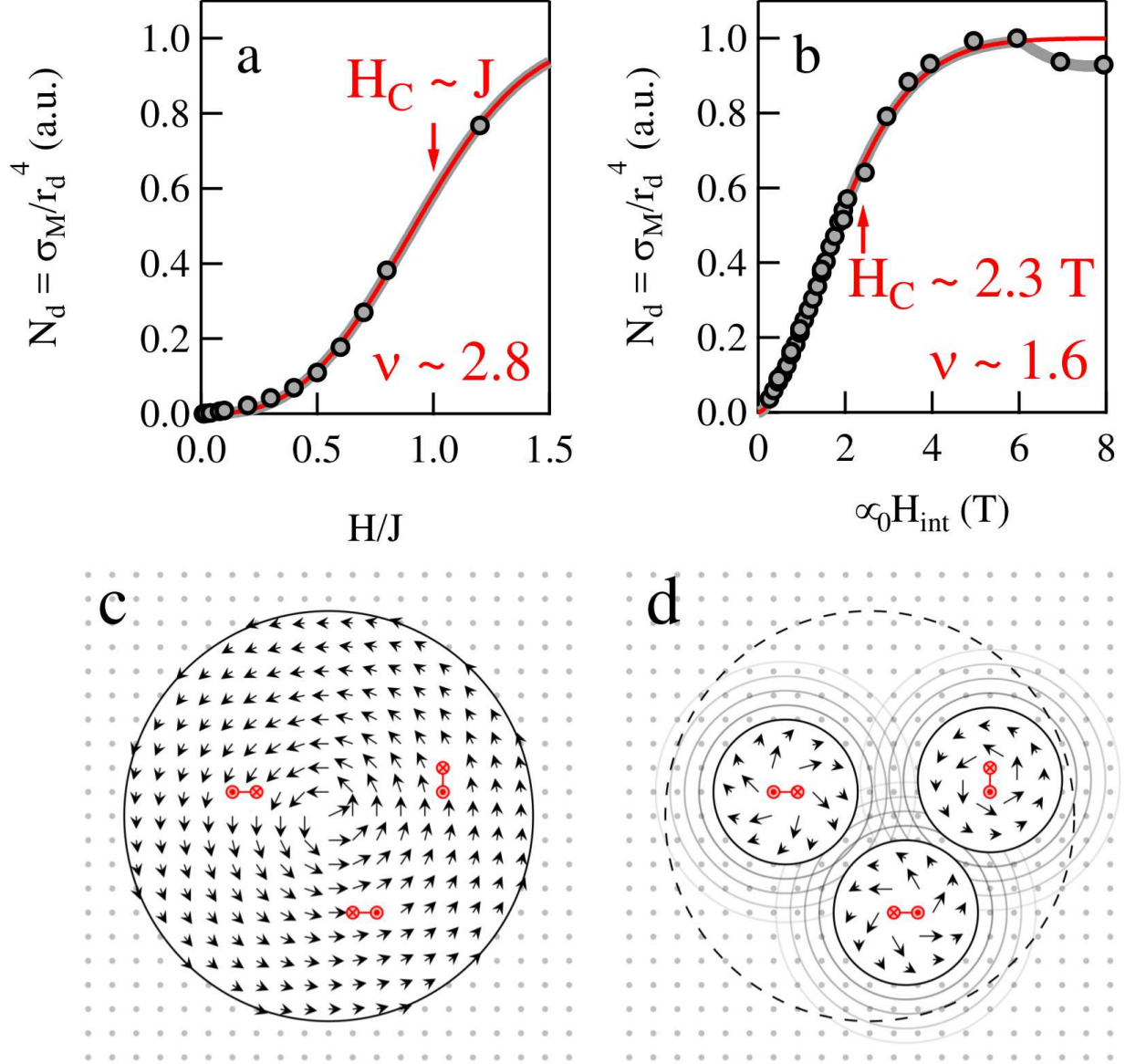


FIG. 15: **(a,b)** Field-dependence of the number of isolated vortex-like defects N_d as seen by MC simulation **(a)** and small-angle neutron scattering **(b)**. In both panels, red lines represent fits of Eq. 4 of main text to the data. **(c,d)** Schematic evolution of the vortex-like defects. **(c)** At low magnetic fields, large vortices encompass several AFM bonds (shown in red). **(d)** With increasing field, they shrink and become singled out, leading to the observed increase of N_d in **(a,b)**.